A Computational Framework for Transmission Risk Assessment of Aerosolized Particles in Classrooms

Kendrick Tan[1,2], Boshun Gao[1], Cheng-Hau Yang[1], Emily L. Johnson[1,3], Ming-Chen Hsu[1], Alberto Passalacqua[1], Adarsh Krishnamurthy[1], Baskar Ganapathysubramanian[1]*

[1] Department of Mechanical Engineering, Iowa State University, Ames, IA 50011, USA

[2] Institute of High Performance Computing, Agency for Science, Technology and Research (A*STAR), Singapore 138632, Singapore

[3] Department of Aerospace and Mechanical Engineering, University of Notre Dame, Notre Dame, IN 46556, USA

* Corresponding Author Email: baskarg@iastate.edu

Abstract

Infectious airborne diseases like the recent COVID-19 pandemic render confined spaces high-risk areas. However, in-person activities like teaching in classroom settings and government services are often expected to continue or restart quickly. It becomes important to evaluate the risk of airborne disease transmission while accounting for the physical presence of humans, furniture, and electronic equipment, as well as ventilation. Here, we present a computational framework and study based on detailed flow physics simulations that allow straightforward evaluation of various seating and operating scenarios to identify risk factors and assess the effectiveness of various mitigation strategies. These scenarios include seating arrangement changes, presence/absence of computer screens, ventilation rate changes, and presence/absence of mask-wearing. This approach democratizes risk assessment by automating a key bottleneck in simulation-based analysis–creating an adequately refined mesh around multiple complex geometries. Not surprisingly, we find that wearing masks (with at least 74% inward protection efficiency) significantly reduced transmission risk against unmasked and infected individuals. While the use of face masks is known to reduce the risk of transmission, we perform a systematic computational study of the transmission risk due to variations in room occupancy, seating layout and air change rates. In addition, our findings on the efficacy of face masks further support use of face masks. The availability of such an analysis approach will allow education administrators, government officials (courthouses, police stations), and hospital administrators to make informed decisions on seating arrangements and operating procedures.

Keywords

Risk Assessment | Aerosolized Particulate Transfer | CFD | Classroom

1 Introduction

The COVID-19 pandemic has irreversibly changed how we consider transmission risk in indoor environments. The physical distancing or six-foot rule [1, 2], for instance, is a guideline that does not account for small aerosol droplets that are continuously mixed through an indoor space. This is especially alarming considering that airborne transmission–via small aerosolized particles–of COVID-19 is widely recognized [3–6]. The distribution of aerosolized particles depends on a dizzying array of factors, including ventilation and air filtration rates, airflow patterns in the indoor space that are impacted by furniture, thermal fluxes on the room facade, and respiratory activity of the inhabitants. While tools for risk assessment have recently been developed [7–9], most such tools make significant assumptions on the indoor environment (well-mixed air, no thermal plumes from equipment and occupants) and the respiratory activity (exhalation of virion particles). Thus, while conventional tools may indicate that a particular room is low-risk ***on average***, there

may be specific locations in the room with significantly higher risk for transmission–for example, in areas where local recirculation causes limited air exchange with the outside environment. Location-specific risk assessment becomes especially important if individuals are seated in such locations for extended periods, increasing their cumulative exposure time, such as our K-12 students, public service workers, and essential workers. For instance, courthouse activities require participants (judges, clerks, petitioners, jurors) to remain sedentary over long periods. Similarly, most classroom activities require students to remain seated for extended periods. In such scenarios, it becomes imperative to identify if specific locations have higher risk and rank among alternate arrangements.

Consider the case of aerosols (with particles <10 μm), which exhibit significantly larger traveling distances [10]. These respiratory particles are suspended in a warm and moist puff cloud, which increases the traveling distance of the respiratory particles before they settle onto surfaces due to gravity [11]. The additional distance traveled by small respiratory droplets can also be attributed to expired jets (even with the use of face masks) [12]. The transport of the small respiratory particles within an enclosed space may also be complicated by the flow field induced by ventilation systems and the thermal plumes from computers and human occupants [13]. The tendency of droplets to remain airborne may be further affected by ambient flow characteristics such as the flow speed, turbulence intensity, direction, temperature, and relative humidity [14]. Such small particles do not generally undergo break-up. Apart from their potential to become airborne, small respiratory particles also can penetrate deeper into the human lower respiratory tract [15] and have higher infectivity than larger cough droplets [16]. Maintaining a physical distance from an infected individual does not entirely protect susceptible individuals from inhaling enough respiratory aerosols to cause infection [14]. Hence, there is a pressing need to accurately model the transport of virion-laden aerosols, especially in indoor settings, to identify (and mitigate) risk zones.

In this context, high-fidelity fluid simulations provide a practical approach to evaluate various seating and operating scenarios, identify risk factors, and assess mitigation strategies. Ideally, such approaches need to be rapidly deployable, customizable to specific scenarios (geometry, occupant conditions, environmental conditions, ventilation), and suitable for extracting reliable best practices. A major challenge in this type of simulation is the mesh generation step. The resolution and quality of the mesh are intimately related to the overall accuracy of the simulation. Although mesh generation is a fundamental part of numerical approaches, creating high-quality meshes continues to be a significant bottleneck in the overall workflow. This restriction is exacerbated when considering adaptivity and becomes exceptionally challenging in the presence of an arbitrarily shaped geometric object. Streamlining this workflow is one of the components of the NASA 2030 computational fluid dynamics (CFD) milestone towards the goal of conducting overnight large-eddy simulations (LES) [17]: *"Mesh generation and adaptivity continue to be significant bottlenecks in the CFD workflow."*

Here, we deploy a framework that can democratize the execution of such risk assessment studies. This framework consists of (a) immersogeometric carved-out analysis that allows automated consideration of geometrically complex objects in a principled analysis platform [18], (b) a massively parallel octree-based mesh generator that rapidly constructs high-quality meshes [19], (c) a detailed flow physics simulation (LES) to produce accurate flow features [20], (d) a coupled thermal solver to account for the thermal plumes produced by humans and electronics [21], and (e) a passive scalar transport model that accounts for the distribution of virion-laden aerosols. We illustrate this framework by assessing the risk of transmission across various seating plans, operating conditions, and aerosol source locations in a canonical classroom setting, specifically a room where several of us teach (Figure 7). The availability of such an analysis approach will allow education administrators (K-12, university), federal/state/local government officials (courthouses, police stations), and hospital administrators to make informed decisions on seating arrangements and operating procedures.

2 Computational Framework

We adopt an Eulerian-Eulerian-based Finite Element Method (FEM) approach with linear basis functions and variational multiscale (VMS) [21, 22] framework to discretize and solve the governing equations for the flow and transport of the virion particles. The momentum and heat transfer equations are solved concurrently with an in-house Navier-Stokes Heat Transfer (NS-HT) solver to compute the time evolution of the flow field within the classroom. A temporally averaged flow field in the classroom is then obtained across multiple time steps after the flow field reaches a statistically steady state. The time-averaged flow field is then used as an advection field to compute the transport of the virion-laden aerosols in the advection-diffusion (AD) solver. The simulation workflow is depicted in a schematic shown in Figure 1.

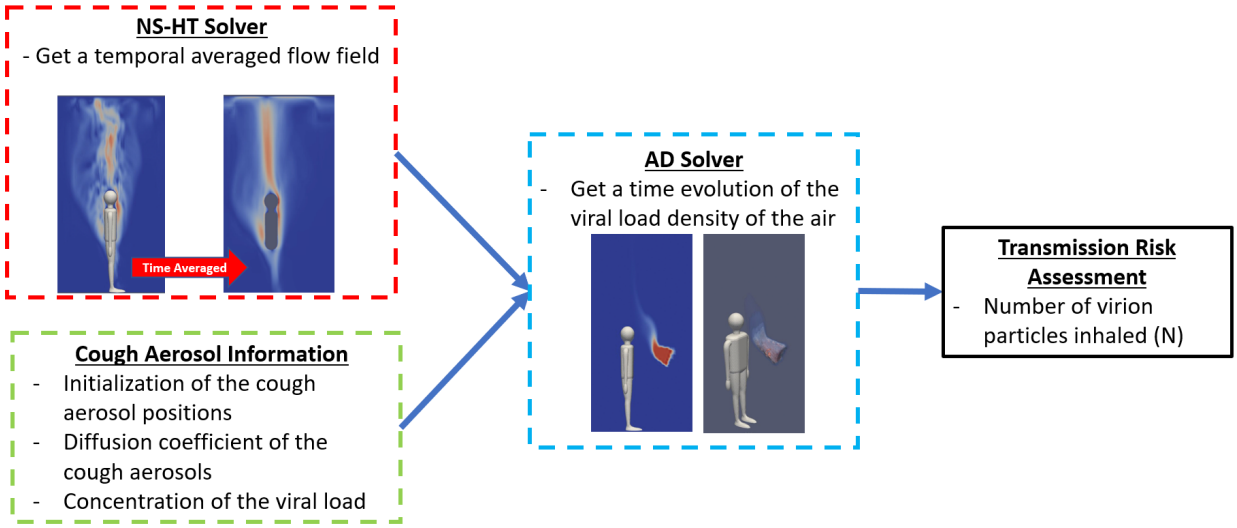

Figure 1: *Simulation workflow to compute the transmission risk.*

Information about the virion-laden aerosols (such as the initialization of their position due to a cough, viral load density, and diffusion coefficient) is also required as inputs to the AD solver. The virion-laden aerosols are modeled as a continuum and considered a passive scalar in the AD solver. The backward differentiation formula 2 (BDF2) is used as the time-stepping scheme in the solution of the governing equations. Information about the viral load density of the air, obtained from the solution of the AD solver, is then post-processed to compute the number of virion particles that would be inhaled at every location within the classroom (N). The magnitude of N at every location within the classroom is compared with the minimum infective dose (MID) for the transmission risk assessment.

We use CAD models (STL files) of desks, chairs, and monitors to realistically represent various solid (and slender) objects that can impact the flow patterns. We utilize STL files of mannequins to represent human subjects. These STL files allow straightforward reconfiguration and exploration of various scenarios. We consider a fall semester operating condition and take into account the heat flux from both humans and electronic equipment.

2.1 Related Work

The well-mixed room (WMR) model is a mathematical model that predicts the probability of airborne pathogen transmission within an enclosed space based on the time evolution of the airborne pathogen concentration. The WMR model computes the concentration of the airborne pathogen based on a simple mathematical model that relates the rate of change of the pathogen concentration to various parameters of the venue under consideration, such as the number of occupants, size of the room, shedding rate of virion particles from the infected host(s), rate of removal of pathogens from artificial/natural ventilation, rate of

destabilization of the pathogen, etc. [23]. However, several assumptions are made in the WMR model, making it invalid under more complicated and real-life scenarios. Furthermore, the WMR model is incapable of computing the risk of pathogen transmission in the spatial domain.

Hence, most computational-based transmission risk assessment models focus on predicting the transport of the pathogen-laden aerosols by a computed flow field governed by the Navier-Stokes equations. In particular, most computational studies adopt the Eulerian-Lagrangian approach to compute the transport of respiratory droplet particles in air [24–27]. In this approach, the fluid phase (air) is solved as a continuous phase, while the motion of the discrete phase (respiratory droplets) is computed based on the flow characteristics of the fluid phase and the properties of the discrete phase. Since the size of a respiratory droplet affects its transport properties (such as its molecular diffusion coefficient and drag coefficient [28]) and viral load [29], information about the size distribution of the respiratory droplets is required for the Eulerian-Lagrangian approaches. However, such information varies vastly across the cited literature [15, 30–34]. This difference can be attributed to the different (and possibly wrong) techniques and assumptions involved with the measurements of the respiratory droplets [35]. Using an unsuitable droplet size distribution in an Eulerian-Lagrangian approach would imply an error in the predicted transport path of respiratory droplets and, therefore, the assessment of the transmission risk. Furthermore, since approximately $O(10^5)$ airborne particles may be released in a single cough [36], it may be computationally expensive to use the Eulerian-Lagrangian approach to predict the particle transport, especially in a complex flow field.

In the alternative Eulerian-Eulerian approach, the fluid phase and the airborne respiratory virion particles are both treated as continuous phases in the solution of their respective governing equations. This approach has been used infrequently for the prediction of pathogen transmission for SARS-CoV-2 so far. The Eulerian-Eulerian approach provides users with a lowered computational cost, which is beneficial for parameter studies where multiple scenarios need to be simulated to analyze the effect of the various factors.

The discretization of the computational domain for most SARS-CoV-2 transmission simulations is performed with an unstructured tetrahedral body-fitted mesh. Ideally, structured or hexahedral body-fitted meshes would be desired for the solution of a discretized domain due to the generally lowered cell count, better convergence rate, and lowered computational cost compared to tetrahedral meshes [37]. However, the generation of structured or hexahedral meshes requires significantly more time and effort than that of unstructured mesh generation, especially for a computational domain with geometric complexities [38]. Furthermore, body-fitted meshes (both unstructured and hexahedral) require a certain degree of manual effort to design a discretized computational domain that conforms to the surface of the complicated geometries involved [39]. Hence, discretizing a computational domain with a body-fitted mesh can be computationally expensive and cumbersome, especially when multiple geometrically different computational domains have to be adopted for a parameter study.

Tree-based adaptive mesh generation would be a suitable approach for the creation of the meshes in a parameter study [19, 20]. This mesh generation approach involves immersing the geometries into a background mesh before carving out the mesh that resides within the geometries. The carved-out space in the background mesh represents the region occupied by the geometries, while the effect of the geometries' surfaces is represented using the voxelized boundaries. In contrast to unstructured background meshes, the octree-based parallel adaptive mesh is capable of scalability at extreme scales. It also ensures the generation of a high-quality background mesh with a uniform aspect ratio. This method relaxes the requirements for the mesh quality along the boundaries of the immersed geometries. Also, it provides users with a swift method of generating a discretized computational domain, which is essential for the generation of meshes for the multiple geometrically different computational domains required in a parameter study.

In terms of quantifying transmission risk, we observed a generally similar assessment method across the literature. Some authors quantify the risk of transmission in terms of the amount of pathogen released by the carrier [25, 40]. In contrast, others quantify the risk in terms of the number of virion particles being inhaled by susceptible persons [7–9]. The release of virion particles from a carrier does not necessarily result in a transmission unless others inhale the virion particles. However, the inhalation of virion particles does not equate to certainty in disease transmission due to the MID required for susceptible individuals to become infected. Based on a study of the virion exposures for multiple superspreading events, it has been hypothesized that the MID for SARS-CoV-2 infection in susceptible people is 50 particles [23]. Hence, the inhalation of virion particles below the speculated MID into the respiratory system is unlikely to cause an infection.

Since it has been postulated that duration of exposure to a pathogen (in addition to the physical distance from a disease carrier [41]) is another contributing factor to disease transmission [8], the transmission risk assessment should also account for the exposure time. We can fulfill the consideration of exposure time in the transmission risk assessment by relating the risk of transmission to the cumulative sum of the viral load density at the respective position within the considered domain. This can indicate the total number of virion particles inhaled by an occupant at that position over the simulated duration. We can then compare the cumulative amount of virion particles inhaled at a location with the MID to gauge if a susceptible individual is prone to infection.

2.2 Variational Multiscale Formulation

2.2.1 Strong Formulation of the Continuous Problem

Navier-Stokes Equations: Since the Mach Number (Ma) of the flow in a classroom environment is less than 0.3, the flow may be assumed to be incompressible. The Navier-Stokes equations for incompressible flows can be written for a spatial domain $\Omega \subset \mathbb{R}^d$, $d = 2, 3$ and boundary Γ as:

$$\frac{\partial u_i}{\partial t} + \frac{\partial u_i u_j}{\partial x_j} = -\frac{1}{\rho}\frac{\partial P}{\partial x_i} + \frac{1}{Re}\frac{\partial^2 u_i}{\partial x_j \partial x_j} + f_i \tag{1}$$

$$\frac{\partial u_j}{\partial x_j} = 0 \tag{2}$$

where u_i is the i-th component of the velocity vector, f_i is the i-th component of the forcing function that defines the velocity-temperature coupling, P is the pressure, ρ is the flow density, and ν is the kinematic viscosity.

The Boussinesq approximation is used in the incompressible Navier-Stokes equations. This assumes that the density changes in the fluid can be neglected for all terms in the momentum equation except for the body force term defined by the velocity-temperature coupling. Hence, the velocity-temperature coupling can be defined as $f_i = -g_i\,\beta\,(T - T_{ref})$, where g_i is the i-th component of the gravitational acceleration, T is the temperature of the fluid, and T_{ref} is the reference temperature defined as the ambient room temperature.

All the governing equations solved using the in-house code are in nondimensional form. We nondimensionalize the Navier-Stokes equations using the height of the classroom ($L_{ref} = 3.5$ m) as the reference length, the flow velocity at the inlet vents ($U_{ref} = 1.575$ m/s) as the reference velocity, the ratio of the reference length to the reference velocity ($t_{ref} = \frac{L_{ref}}{U_{ref}}$) as the reference time, and the largest temperature difference within the computational domain ($\Delta T = T_H - T_C$) as the reference temperature difference. The nondimensional Navier-Stokes equations to be solved in the in-house code are then given by

$$\frac{\partial u_i^*}{\partial t^*} + \frac{\partial u_i^* u_j^*}{\partial x_j^*} = -\frac{\partial P^*}{\partial x_i^*} + \frac{1}{Re}\frac{\partial^2 u_i^*}{\partial x_j^* \partial x_j^*} + \frac{Gr}{Re^2} T^* z_i \tag{3}$$

$$\frac{\partial u_j^*}{\partial x_j^*} = 0 \tag{4}$$

where $(.)^*$ refers to dimensionless quantities with respect to the reference quantities ($x^* = {}^{x}/_{L_{ref}}, u^* = {}^{u}/_{U_{ref}}, t^* = {}^{t}/_{t_{ref}}, T^* = {}^{T-Tc}/_{\Delta T}$). The dimensionless groups Reynolds number (Re) and Grashof number (Gr) are defined as $Re = {}^{U_{ref}L_{ref}}/_{\nu}$ and $Gr = {}^{g\beta\Delta T L_{ref}^3}/_{\nu^2}$, respectively.

The solution of the Navier-Stokes equations is subjected to the respective Dirichlet and Neumann boundary conditions on the domain boundaries, $\Gamma_{u^*} = \Gamma_{u^*}^D \cup \Gamma_{u^*}^N$, where $\Gamma_{u^*}^D$ represents the boundaries with applied Dirichlet boundary conditions and $\Gamma_{u^*}^N$ represents the boundaries with applied Neumann boundary conditions:

$$u_i^* = (u_i^*)_g \quad \text{on} \quad \Gamma_{u^*}^D \tag{5}$$

$$-P^*\hat{n}_i + \frac{1}{Re}\frac{\partial u_i^*}{\partial x_j^*}\hat{n}_j \quad \text{on} \quad \Gamma_{u^*}^N \tag{6}$$

where $(u_i^*)_g$ is the i-th component of the prescribed velocity at the Dirichlet boundary and $\hat{n}_i$ is the component of the unit normal vector.

Heat Equation: The heat transfer equation for the same domain and boundary can be written as

$$\frac{\partial T}{\partial t} + \frac{\partial T u_j}{\partial x_j} = \alpha \frac{\partial^2 T}{\partial x_j \partial x_j} \tag{7}$$

where T is the temperature and α is the thermal diffusivity of the fluid. When nondimensionalized, the heat equation can be written as

$$\frac{\partial T^*}{\partial t^*} + \frac{\partial T^* u_j^*}{\partial x_j^*} = \frac{1}{Pe_{HT}}\frac{\partial^2 T^*}{\partial x_j^* \partial x_j^*} \tag{8}$$

where the dimensional group Peclet number of heat transfer is defined as $Pe_{HT} = \frac{U_{ref}L_{ref}}{\alpha}$ based on the reference length, reference velocity, and thermal diffusivity of the ambient air at 21.3 °C of $\alpha = 2.177 \times 10^{-5}\ \mathrm{m}^2/\mathrm{s}$. The viscous dissipation in the thermal energy equation can be neglected, since the flow speeds involved are significantly lower than the speed of sound.

The solution of the heat equation is subjected to the respective Dirichlet and Neumann boundary conditions on the domain boundaries, $\Gamma_{T^*} = \Gamma_{T^*}^D \cup \Gamma_{T^*}^N$, where $\Gamma_{T^*}^D$ refers to the boundaries with applied Dirichlet boundary conditions and $\Gamma_{T^*}^N$ represents the boundaries with applied Neumann boundary conditions:

$$T^* = T_g^* \quad \text{on} \quad \Gamma_{T^*}^D \tag{9}$$

$$\frac{1}{Pe_{HT}}\frac{\partial T^*}{\partial x_j^*}\hat{n}_j = h_T^* \quad \text{on} \quad \Gamma_{T^*}^N \tag{10}$$

where T_g^* is the prescribed temperature at the Dirichlet boundary.

Transport Equation for Viral Load Concentration: The virus-laden aerosols are modeled as a continuum where the time evolution of the viral load concentration (in terms of $quanta/\mathrm{m}^3$) is computed from the advection-diffusion equation:

$$\frac{\partial C}{\partial t} + \frac{\partial C u_j}{\partial x_j} = \frac{1}{D_{mol}}\frac{\partial^2 C}{\partial x_j \partial x_j} \tag{11}$$

where C is the viral load concentration and D_{mol} is the molecular diffusion coefficient of the virion-laden aerosols. When nondimensionalized, the advection-diffusion equation can be written as

$$\frac{\partial C^*}{\partial t^*} + \frac{\partial C^* u_j^*}{\partial x_j^*} = \frac{1}{Pe_{AD}} \frac{\partial^2 C^*}{\partial x_j^* \partial x_j^*} \tag{12}$$

where the dimensional group Peclet number of the advection-diffusion transport is $Pe_{AD} = {}^{U_{ref} L_{ref}}/_{D_{eff}}$ based on the reference length, reference velocity, and the effective diffusion coefficient of the particle-laden aerosol.

Since the molecular diffusion coefficient of the aerosols is significantly smaller than the kinetic and turbulent viscosity, the magnitude of the diffusion coefficient used in Pe_{AD} has to be modified to include the effect of eddy mixing [42]. Hence, the effective diffusion coefficient comprises the molecular and eddy diffusivity of the virus-laden aerosols: $D_{eff} = D_{mol} + D_{eddy}$. The eddy diffusivity of the aerosols are defined based on the Smagorinsky Lily Model, $D_{eddy} = ({}^{C_s}/_{Sc})\Delta^2\sqrt{2S_{ij}S_{ij}}$, where $C_s = 0.1$, $\Delta = (\text{cell volume})^{\frac{1}{3}}$, and S_{ij} is the strain rate tensor. The initial viral load concentration is C_{ref}. Unless otherwise specified, we set the properties of the aerosolized fluid to those of water droplets.

The solution of the transport equation for the viral load is similarly subjected to the respective Dirichlet and Neumann boundary conditions on the domain boundaries, $\Gamma_{C^*} = \Gamma_{C^*}^D \cup \Gamma_{C^*}^N$, where $\Gamma_{C^*}^D$ refers to the boundaries with applied Dirichlet boundary conditions and $\Gamma_{C^*}^N$ refers to the boundaries with applied Neumann boundary conditions:

$$C^* = C_g^* \quad \text{on} \quad \Gamma_{C^*}^D \tag{13}$$

$$\frac{1}{Pe_{AD}} \frac{\partial C^*}{\partial x_j^*} \hat{n}_j = h_c^* \quad \text{on} \quad \Gamma_{C^*}^N \tag{14}$$

where C_g^* is the prescribed viral load concentration at the Dirichlet boundary.

The dimensionless groups are defined based on the reference length L_{ref}; reference velocity U_{ref}; and kinematic viscosity and thermal expansion coefficient of ambient air at 21.3 °C, $\nu = 1.540 \times 10^{-5}$ m^2/s, and $\beta = 3.396 \times 10^{-3}\text{K}^{-1}$, respectively.

2.2.2 Weak Formulation of the Governing Equations

Let $\mathcal{V}$ be the space of both the trial and test functions. The variational formulation is stated as follows: Find $\{u_i^*, P^*, T^*\} \in \mathcal{V}$ such that $\forall \{w_i, q, l\} \in \mathcal{V}$,

$$B(\{w_i, q, l\}, \{u_i^*, p^*, T^*\}) - F(\{w_i, q, l\}, \{u_i^*, P^*, T^*\}) = 0 \tag{15}$$

where

$$\begin{aligned}
&B(\{w_i, q, l\}, \{u_i^*, P^*, T^*\}) \\
&= \int_\Omega w_i \frac{\partial u_i^*}{\partial t^*} d\Omega - \int_\Omega \frac{\partial w_i}{\partial x_j^*} u_i^* u_j^* d\Omega + \int_\Omega \frac{1}{Re} \frac{\partial w_i}{\partial x_j^*} \frac{\partial u_i^*}{\partial x_j^*} d\Omega - \int_\Omega \frac{P^*}{\rho} \frac{\partial w_i}{\partial x_i^*} d\Omega \\
&+ \int_\Omega q \frac{\partial u_i^*}{\partial x_i^*} d\Omega \\
&+ \int_\Omega l \frac{\partial T^*}{\partial t^*} d\Omega - \int_\Omega \frac{\partial l}{\partial x_j^*} u_j^* T^* d\Omega + \int_\Omega \frac{1}{Pe_{HT}} \frac{\partial l}{\partial x_j^*} \frac{\partial T^*}{\partial x_j^*} d\Omega
\end{aligned}$$

and

$$
\begin{aligned}
&F(\{w_i, q, l\}, \{u_i^*, P^*, T^*\}) \\
&= \int_\Omega w_i f_i^* d\Omega - \int_{\Gamma_u^N} (w_i u_i^*) u_j^* n_j d\Gamma + \int_{\Gamma_{u^*}^N} w_i (h_u^*)_i d\Gamma \\
&- \int_{\Gamma_{T^*}^N} l T^* u_i^* \hat{n}_i d\Gamma + \int_{\Gamma_{T^*}^N} l h_T^* d\Gamma
\end{aligned}
$$

where F contains the boundary convection and pressure terms, the body force term from the momentum equation, and the convection term from the heat transfer equation.

2.2.3 Semi-Discrete Variational Multiscale Formulation

In the application of variational multiscale theory to the governing equations involved in a buoyancy-driven convection problem [21], the space that contains the trial solution and the weighting functions is separated into coarse and fine subspaces as $\mathcal{V} = \mathcal{V}^h \oplus \mathcal{V}'$, where the superscript h represents the resolved coarse scales being solved by the finite element discretization and the primed variable represents the unresolved fine scales that will be modeled:

$$
\{u_i^*, P^*, T^*\} = \{(u_i^h)^*, (P^h)^*, (T^h)^*\} + \{(u_i')^*, (P')^*, (T')^*\} \tag{16}
$$

$$
\{w, q, l\} = \{w^h, q^h, l^h\} + \{w', q', l'\} \tag{17}
$$

Substituting Equation (16) into (15) and defining the weighting functions as $\{w_i, q, l\} = \{w_i^h, q^h, l^h\}$, the following equation is derived:

$$
\begin{aligned}
&B(\{w_i^h, q^h, l^h\}, \{(u_i^h)^*, (p^h)^*, (T^h)^*\} + \{(u_i')^*, (P')^*, (T')^*\}) \\
&-F(\{w_i^h, q^h, l^h\}, \{(u_i^h)^*, (p^h)^*, (T^h)^*\} + \{(u_i')^*, (P')^*, (T')^*\}) = 0
\end{aligned} \tag{18}
$$

where $\{w_i^h, q^h, l^h\}$ are in a finite-dimensional space. Equation (18) is a finite-dimensional system of equations, where the coarse-scale variables $\{w_i^h, q^h, l^h\}$ are the unknowns to be solved and are dependent on the fine-scale variables. Since the fine scales are not resolved, their effect on the coarse-scale fields must be modeled.

The domain Ω is decomposed into a collection of N_{el} elements (represented by Ω^e), where $\Omega = \cup_{e=1}^{N_{el}} \Omega^e$. With reference to the variational multiscale formulation developed by Bazilevs et al. [22], a semi-discrete variational multiscale formulation for the Navier-Stokes and heat transfer equations can be defined as the following:

$$
\begin{aligned}
&B^{VMS}(\{w_i^h, q^h, l^h\}, \{(u_i^h)^*, (P^h)^*, (T^h)^*\}) \\
&-F^{VMS}(\{w_i^h, q^h, l^h\}, \{(u_i^h)^*, (P^h)^*, (T^h)^*\}) = 0
\end{aligned} \tag{19}
$$

Find $\{(u_i^h)^*, (P^h)^*, (T^h)^*\} \in \mathcal{V}^h$ such that $\forall \{w_i^h, q^h, l^h\} \in \mathcal{V}^h$, where

$$
\begin{aligned}
&B^{VMS}(\{w_i^h, q^h, l^h\}, \{(u_i^h)_i^*, (P^h)^*, (T^h)^*\}) \\
&= \int_\Omega w_i^h \frac{\partial (u_i^h)^*}{\partial t^*} d\Omega - \int_\Omega w_i (u_j^h)^* \frac{\partial (u_i^h)^*}{\partial x_j^*} d\Omega + \int_\Omega \frac{1}{Re} \frac{\partial w_i^h}{\partial x_j^*} \frac{\partial (u_i^h)^*}{\partial x_j^*} d\Omega - \int_\Omega (P^h)^* \frac{\partial w_j}{\partial x_j^*} d\Omega \\
&+ \int_\Omega q^h \frac{\partial (u_j^h)^*}{\partial x_j^*} d\Omega \\
&+ \int_\Omega l^h \frac{\partial (T^h)^*}{\partial t^*} d\Omega + \int_\Omega l^h (u_j^h)^* \frac{\partial (T^h)^*}{\partial x_j^*} d\Omega + \int_\Omega \frac{1}{Pe_{HT}} \frac{\partial l^h}{\partial x_j^*} \frac{\partial (T^h)^*}{\partial x_j^*} d\Omega \\
&- \sum_{e=1}^{N_{el}} \int_\Omega \left((u_j^h)^* \frac{\partial w_i^h}{\partial x_j^*} (u_i')^* + \frac{\partial q^h}{\partial x_j^*} (u_j')^* \right) d\Omega - \sum_{e=1}^{N_{el}} \int_\Omega (u_j^h)^* \frac{\partial l^h}{\partial x_j^*} (T')^* d\Omega - \sum_{e=1}^{N_{el}} \int_\Omega \frac{\partial (P')^*}{\partial x_j^*} \frac{\partial w_j^h}{\partial x_j^*} d\Omega \\
&+ \sum_{e=1}^{N_{el}} \int_\Omega w_i^h (u_j')^* \frac{\partial (u_i^h)^*}{\partial x_j^*} d\Omega - \sum_{e=1}^{N_{el}} \int_\Omega \frac{\partial w_i^h}{\partial x_j^*} d\Omega + \sum_{e=1}^{N_{el}} \int_\Omega l^h (u_j')^* \frac{\partial (T^h)^*}{\partial x_j^*} d\Omega - \sum_{e=1}^{N_{el}} \int_\Omega \frac{\partial l}{\partial x_j^*} (u_j')^* (T')^* d\Omega
\end{aligned}
\tag{20}
$$

and

$$
\begin{aligned}
&F^{VMS}(\{w_i^h, q^h, l^h\}, \{(u_i^h)^*, (P^h)^*, (T^h)^*\}) \\
&= \int_\Omega w_i^h (f_i^h)^* d\Omega + \sum_{e=1}^{N_{el}} \int_\Omega w_i^h (f_i')^* d\Omega + \int_{\Gamma_{u^*}^N} w_i^h (h_u^*)_i d\Gamma + \int_{\Gamma_{T^*}^N} l^h h_T^* d\Gamma
\end{aligned}
\tag{21}
$$

where $(f_i')^* = -\frac{g_i \beta (T')^* L_{ref}}{U_{ref}^2}$.

The terms in the second, third, and fourth lines of Equation (20) correspond to the Galerkin form of the governing equations, $B(\{w_i^h, q^h, l^h\}, \{(u_i^h)^*, (P^h)^*, (T^h)^*\})$, from Equation (15). The terms in the fifth line of Equation (20) correspond to the stabilization terms which comprise the streamline-upwind Petrov-Galerkin (SUPG) and the pressure-stabilizing Petrov-Galerkin (PSPG) stabilization terms [43, 44]. The last line of Equation (20) corresponds to the terms generated by the VMS formulation [22]. The solution for the fine-scale variables can be modeled as a linear approximation based on the residuals of the coarse-scale solutions [22], where the fine-scale variables can be defined as the following:

$$(u_i')^* = -\tau_M r_M(\{(u_i^h)^*, (P^h)^*, (T^h)^*\}) \tag{22}$$

$$(P')^* = -\tau_C r_C((u_i^h)^*) \tag{23}$$

$$(T')^* = -\tau_E r_E(\{(u_i^h)^*, (T^h)^*\}) \tag{24}$$

where

$$(r_M)_i = \frac{\partial u_i^*}{\partial t^*} + (u_j^h)^* \frac{\partial (u_i^h)^*}{\partial x_j^*} + \frac{\partial (P^h)^*}{\partial x_i^*} - \frac{1}{Re} \frac{\partial^2 (u_i^h)^*}{\partial x_j^* \partial x_j^*} - (f_i^h)^* \tag{25}$$

$$r_C = \frac{\partial (u_j^h)^*}{\partial x_j^*} \tag{26}$$

$$r_E = \frac{\partial (T^h)^*}{\partial t^*} + (u_j^h)^* \frac{\partial (T^h)^*}{\partial x_j^*} - \frac{1}{Pe_{HT}} \frac{\partial^2 (T^h)^*}{\partial x_j^* \partial x_j^*} \tag{27}$$

$$\tau_M = \left(\frac{4}{(\Delta t^*)^2} + (u_j^h)^* G_{ij} (u_i^h)^* + \frac{C_M}{Re^2} G_{ij} G_{ij} \right)^{-\frac{1}{2}} \tag{28}$$

$$\tau_C = (\tau_M g_j g_j) \tag{29}$$

$$\tau_E = \left(\frac{4}{(\Delta t^*)^2} + (u_j^h)^* G_{ij} (u_i^h)^* + \frac{C_E}{Pe_{HT}^2} G_{ij} G_{ij} \right)^{-\frac{1}{2}} \tag{30}$$

and

$$G_{ij} = \frac{\partial \xi_k}{\partial x_i^*} \frac{\partial \xi_k}{\partial x_j^*} \tag{31}$$

$$g_i = \sum_{j=1}^{d} \frac{\partial \xi_j}{\partial x_i^*} \tag{32}$$

where $(r_M)_i$, r_C, and r_E are the residuals from the solution of the momentum equation in the i-th direction, continuity equation, and energy equation, respectively. C_M and C_E are positive constants, both of which are set to 36 for all simulations. These values are standard values often used in VMS formulations, and are derived from the theory of stabilization (specifically, element-wise inverse estimates [45, 46]). G_{ij} and g_i are mesh-dependent quantities that are involved with the mapping of physical elements to the isoparametric elements.

2.3 Octree-Based Adaptive Discretization

Conventional body-fitted meshing is both case-specific and labor-intensive to generate. In this study, several geometrically different computational domains with different mesh requirements are required due to the presence of varying objects (such as additional computers or mannequins) placed within the computational domain. Hence, we use an incomplete octree-based adaptive discretization approach for the mesh generation in the computational domains used in this study [19, 20]. The generation of the incomplete octree-based mesh begins with creating a cuboid background mesh composed of cubic elements. Then, a water-tight manifold of the bodies in the computational domain (such as the mannequins, tables, and computers) is

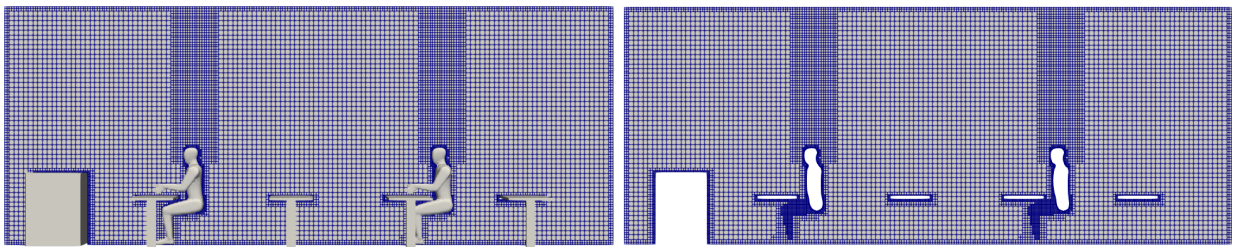

Figure 2: *Various solid objects (mannequins, desks, tables, computers) are placed in the computational domain, and the background mesh is carved out and successively refined. This produces an incomplete octree-based mesh of the computational domain (right).*

immersed in the background mesh. Since the elements of the background mesh in the interior of the manifold are not involved in the numerical solutions of the governing equations, they are removed to reduce the memory footprint required, generating a "carved out" domain in the background mesh. Then, the respective strong boundary conditions for the various governing equations are applied onto the surface of the carved-out region, as shown in Figure 2. This mesh generation process is fully automated, and no manual geometry or mesh cleanup is required. The degree of mesh density of the cubic elements within the octree-based grids is defined by *level*. Each cubic element has a length of $\frac{\max(domain)}{2^{level}}$, where $\max(domain)$ is the length of the longest edge of the computational domain. The degree of mesh density may be increased in specified regions and near the carved-out domains by subdividing the coarser elements in each axis.

2.4 Representation of the Region Occupied by Respiratory Aerosols

Most of the existing computational studies conducted on the transport of the cough aerosols from infected hosts are based on the release of virion particles (for Lagrangian approach [27]) or a specified concentration boundary condition (for an Eulerian approach [9]) at a breathing organ (the nose/ mouth). However, it will be computationally expensive to determine the initial evolution of the cough cloud before its propagation into the ambiance. Such an approach can be expensive, especially for a parameter study where multiple simulations have to be conducted based on several varied factors. However, there is available informative literature that describes the shape, orientation, and properties of the expired cloud during various exhalation processes [10, 30, 47]. Hence, we tap into these resources as inputs for our computational study on the scalar transport and propagation of the cough aerosols throughout the computational domain. This approach allows us to reduce computational costs without compromising the accuracy of the results.

When an individual coughs, a turbulent cloud of buoyant gas with suspended respiratory particles is exhaled from the mouth. This can be approximated by a conical shape[1]. The size, shape, and orientation of the cough cloud can be defined based on parameters such as the entrainment coefficient (α'), coughing angle (θ), and size of the mouth (see Figure 3a) [10].

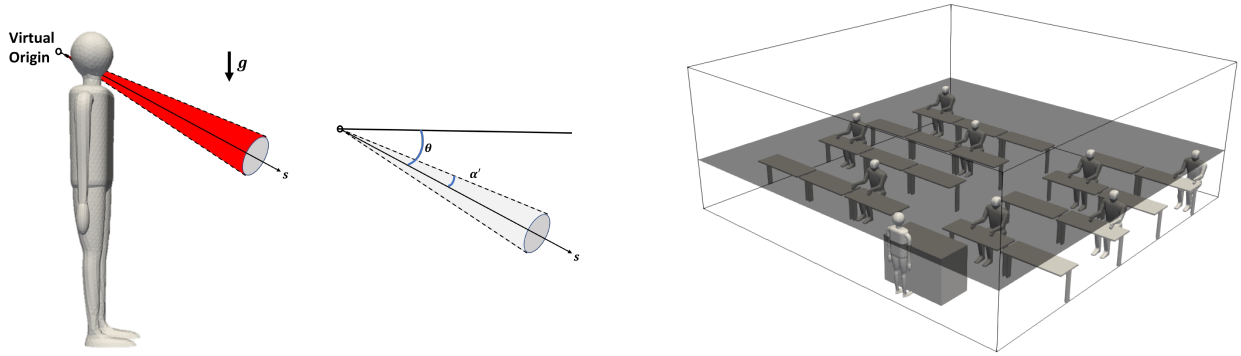

(a) *Cone-shaped region occupied by respiratory droplets after a coughing event. This region serves as the initial condition for concentration distribution.*

(b) *The transmission risk is quantified and visualized on a horizontal plane at breathing height for seated individuals. This plane is shown for a particular seating configuration.*

Figure 3: *Modeling the respiratory droplets and their monitoring plane.*

For this computational study, we assume that the airborne virion aerosols released from a cough are homogeneously distributed throughout the cough cloud before they are subjected to advective and diffusive transport in the AD solver. The region occupied by the cough cloud is defined with a nondimensional viral load density of $C^* = 1$. The reference concentration can be defined based on the known viral load density of the cough cloud.

[1] Bourouiba et al. [10] draw an analogy between a cough and sneeze with jets and plumes.

A single cough from an infected host may release as many as 1.23×10^5 copies of SARS-CoV-2 viruses that can remain airborne after 10 seconds [48]; 94% of these can be effectively blocked by a surgical face mask [49]. The flow resistance of face masks also impedes the spread of the cough cloud from the infected individual into the surroundings [50]. The cough cloud released by the infected individual can be defined using an entrainment coefficient of $\alpha' = 0.2116$ radians, downward coughing angle of $\theta = 23.9°$, and a circular mouth area of $3.4\ \mathrm{cm}^2$ [10], with an extent of 70 cm for an unmasked cougher and 35 cm for a masked cougher [24].

2.5 Metric for Risk Assessment

The risk of infection in the classroom can be quantified by the amount of virion particles inhaled by susceptible individuals at various locations within the classroom relative to that of the SARS-CoV-2 carrier. The number of virion particles, N, drawn into the body with one inhalation breath can be calculated as the product of $C(t)$ the concentration of virion particles in the air being inhaled and V_b the volume of one inhalation. The magnitude of V_b can be defined as 500 ml based on tidal breathing [51].

As noted earlier, we seek to assess risk due to a single cough event over a finite time interval. This is the most conservative estimate of the risk of transport of aersolized particles. Since we are considering scalar transport of the aerosolized particles, one could evaluate the impact of multiple coughing events by adding multiple temporally separated individual coughing events.

The total amount of inhaled virus-laden particles that are cumulatively inhaled at a position over a duration T can be calculated based on

$$N = \int_0^T C(t)\dot{V}_b \, dt \tag{33}$$

where $\dot{V}_b$ is the continuous inhalation rate for humans with an average rate of $1.33 \times 10^{-4}\mathrm{m}^3/\mathrm{s}$, based on 12 to 16 breaths per minute [52]. We consider a 15 minute interval ($T = 900s$) in our simulations. This is informed by ASHRAE[2] Standards, specifically 62.1 and 62.2, which provide recommendations on minimum outdoor ventilation rates for various buildings. Equation (33) is numerically evaluated as

$$N \approx \sum [C(t)\dot{V}_b \, \Delta t] = \dot{V}_b \times \Delta t \times \sum [C(t)]. \tag{34}$$

Although the MID of SARS-CoV-2 is currently unknown (as of early 2022), it is hypothesized to be approximately 50 based on a well-mixed room modeling of 20 super spreading events [23]. Hence, regions with contours of inhaled virion particles with a count greater than 50 would imply that susceptible individuals risk infection if their breathing organs (mouth or nose) reside within these regions. A horizontal slice of the contour for the inhaled particle count is taken at the height of $1.25\mathrm{m}$ to evaluate the transmission risk of the seated occupants. This height corresponds to the location of the breathing organs of the mannequins (see Figure 3b). Based on this risk assessment metric, we can identify the regions where occupants can be susceptible to SARS-CoV-2 viral infection.

3 Validation of Simulation Code

We validated the computational framework against benchmark canonical flow problems.

3.1 Flow Over a Heated Sphere

Since this study aims to analyze the effect of thermally generated flows from heated bodies with prescribed Dirichlet boundary conditions, we validated the approach by examining the results obtained for the heat fluxes off of a heated body. This validation was conducted for the case of a cooling flow across a heated sphere.

[2] *American Society of Heating, Refrigerating and Air-Conditioning Engineers*

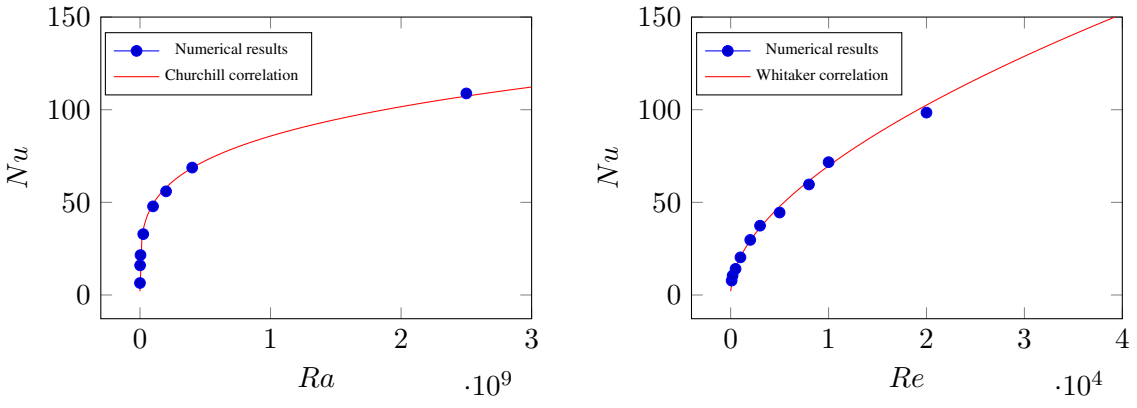

(a) *Free convection.* **(b)** *Forced convection.*

Figure 4: *Comparison of the numerical results obtained for Nu with the empirical correlations for free and forced convection over a heated sphere.*

	Ra	**Empirical Nu**	**Computed Nu**
Free Convection	1.0×10^4	6.71	6.48
	1.0×10^6	16.9	16.0
	4.0×10^6	23.1	21.5
	2.5×10^7	35.3	32.8
	1.0×10^8	49.1	47.8
	2.0×10^8	58.0	55.9
	4.0×10^8	68.6	68.8
	2.5×10^9	107	109
	Re	**Empirical Nu**	**Computed Nu**
Forced Convection	100	7.29	7.77
	200	9.71	10.5
	500	14.7	14.1
	1000	20.6	20.3
	2000	29.4	29.7
	3000	36.4	37.4
	5000	47.8	44.5
	8000	61.8	59.7
	1.0×10^4	69.8	71.7
	2.0×10^4	103	98.4
	5.0×10^4	173	156

Table 1: *Comparison of numerical and empirical Nu for free and forced convection*

The Nusselt number ($Nu = {}^{hD}/_{k}$) represents the dimensionless temperature gradient on the surface of a sphere with diameter D. The surface-averaged Nu is computed based on various Reynolds numbers ($Re = {}^{UD}/_{\nu}$) for forced convection. We assumed an ambient flow velocity of U across the sphere and Rayleigh number $Ra = {}^{g\beta\Delta T D^3}/_{\nu\alpha}$ for free convection of a heated sphere placed in a quiescent fluid.

Let Pr be the Prandtl number. The numerical result obtained for the Nu of the heated sphere is compared to the empirical formula defined for both the free convection of a cooling flow past a heated sphere [53] as $Nu = 2 + \frac{0.589 Ra^{\frac{1}{4}}}{[1+(\frac{0.469}{Pr})^{\frac{9}{16}}]^{\frac{4}{9}}}$ and for forced convection [54] as $Nu = 2 + (0.4Re^{\frac{1}{2}} + 0.06Re^{\frac{2}{3}})Pr^{0.4}$, in Figure 4a and Figure 4b, respectively (see also Table 1). This substantiates the solver's capabilities in computing the temperature gradient and heat fluxes at the surface of the heated bodies within the computational domain.

3.1.1 Thermal Plume Generated by a Mannequin

Since we are interested in investigating the effect of the flow generated by thermally heated bodies, we validate the numerical solution for the velocity field of a thermal plume. A study of the thermal plume generated by a mannequin by Craven and Settles[55] is referenced for this particular validation.

Due to the heat generated by the mannequin, the temperature of the air around the mannequin body increases, and its density decreases relative to the ambient air. The decrease in density drives the air around the mannequin upward, generating a natural convective flow above the mannequin. The vertical flow generated above the mannequin due to buoyancy becomes a thermal plume.

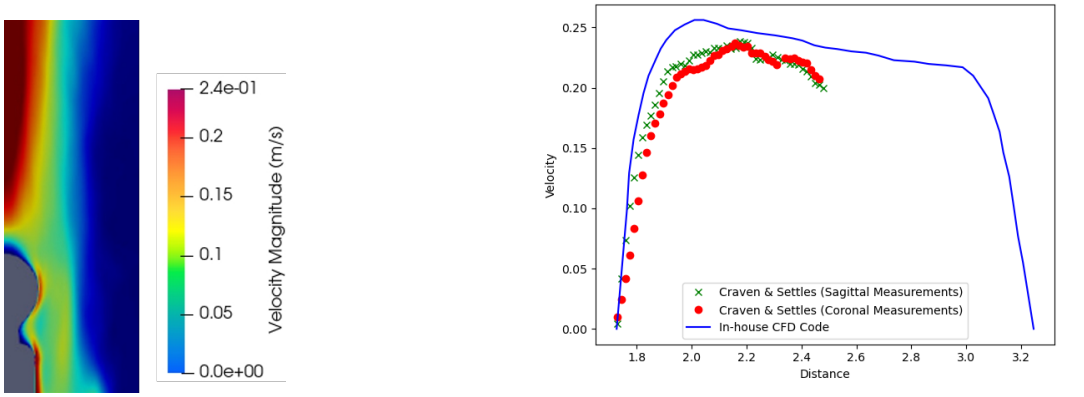

(a) *Velocity contour from our in-house code matches the benchmark case, similar to the results in Fig. 11 from Craven and Settles [55].*

(b) *Comparison plot of the thermal plume above mannequin with the benchmark case [55].*

Figure 5: *Comparison of the numerical results of velocity of the thermal plume above a mannequin with Craven and Settles [55].*

A mannequin with a height of 1.73 m and constant surface temperature of 26.6°C is placed in the middle of a cylindrical domain with a radius 5 m and height 3.25 m. The ambient temperature of the computational domain is 21.3°C. Upon reaching a statistically steady-state solution, the time-averaged solution for the velocity in the thermal plume obtained from the in-house CFD solver is then validated against the results of Craven and Settles [55] (as shown in Figure 5a and Figure 5b). While there is a good qualitative agreement between our results and those reported in Craven and Settles [55], there is a quantitative difference in the thermal plume, especially above the mannequin head ($\approx$12%) at 2 m. This difference can be attributed to the differences in replicating the exact experimental subject, such as the shape of the mannequin and the effect of the clothing insulation. Likewise, Craven and Settles [55] also used a simplified mannequin in their numerical simulations, which omitted some features of the experimental subject.

3.1.2 Advective and Diffusive Transport of Aerosols

The advection-diffusion solver (Section 2.2.1) is used to compute the transport of the virion-laden aerosols with a pre-calculated velocity field. The in-house advection-diffusion solver is validated with a problem that involves the two-dimensional advection of a concentration field (the cosine hill problem). When diffusion is set to a negligibly small value, the concentration field is transported by the underlying velocity. We evaluate the height of the concentration hill after it undergoes one full rotation ($T = 1$). Under zero diffusion, the analytical maximum concentration is 1.00, while the analytical minimum concentration is 0.

The computational domain is $[0, 0.5] \times [0, 0.5]$, and the divergence-free constant velocity field is

$$(u, v) = (sin(2\pi x)cos(2\pi y), -cos(2\pi x)sin(2\pi y)) \tag{35}$$

where u and v are the velocity components in the x- and y-directions, respectively. The initial concentration

Levels	5	6	7	8	Analytical
Minimum	-0.0961	-0.0466	-0.0191	-0.0084	0
Maximum	0.8281	0.9751	0.9982	0.9999	1.000

Table 2: *Minimum and maximum values of cosine-hill problem.*

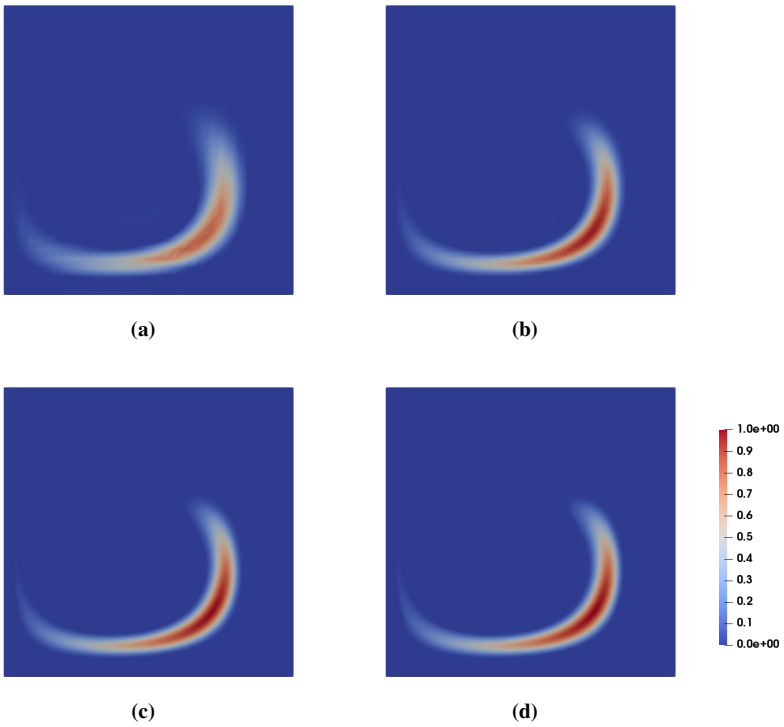

Figure 6: *Contours of concentration field in a two-dimensional rotating velocity field at $T^* = 1$ at a mesh refinement (a) level = 5, (b) level = 6, (c) level = 7, (d) level = 8.*

field was defined as

$$c_0(x,y) = \begin{cases} \frac{1}{4}(1+cos\pi\frac{x-x_c}{\sigma})(1+cos\pi\frac{y-y_c}{\sigma}) & (x-x_c)^2+(y-y_c)^2 \leq \sigma^2 \\ 0 & otherwise \end{cases} \tag{36}$$

where $(x_c, y_c) = (0.375, 0.375)$ is the center of the cosine hill and $\sigma = 0.1$.

Four cases with increasing grid-refinement levels are simulated, from level 5 to level 8, respectively. The Backward Difference Formula (BDF2) time-stepping scheme is used, and the maximum Courant-Friedrichs-Lewy (CFL) number for the cases is kept at 0.3. The diffusion coefficient $1/Pe$ is defined as 10^{-8} for the cases, which suggests that this is close to a pure convection problem. The results for the concentration field at the final time $T = 1$ are shown in Figure 6. A significant difference in the solution from low discretization Figure 6a to moderate discretization Figure 6c is clearly seen. However, beyond this discretization Figure 6c and Figure 6d there is not much difference.

To obtain a quantitative comparison, we then computed the minimum and maximum of the solutions from the four grids in Table 2. Under pure advection, the analytical maximum is 1.00, while the analytical minimum is 0. Deviation of the maximum from 1.0 indicates the impact of numerical diffusion introduced by spatial discretization as well as temporal discretization, while a minimum below 0 suggests overshoot. As the mesh is refined, it is clear that the BDF2 scheme can solve the advection-diffusion problem without the extra introduction of numerical diffusion and very little overshoot.

4 Classroom Simulations

4.1 Computational Setup

4.1.1 Computational Domain and Boundary Conditions

For demonstrating the efficacy of our framework, we consider a typical university classroom that will be employed to investigate the risk of virus transmission. Figure 7a shows the classroom environment prior to the COVID-19 pandemic. As shown in Figure 7b, the room has a length of 9 m, a width of 9 m, and a height of 3.5 m with a ventilation system with eight vents (four inlet vents and four outlet vents) installed on the ceiling. The occupants are modeled using labeled mannequins (Figure 7c). We consider several scenarios and evaluate transmission risk. In particular, we consider the following five scenarios: (a) changing seating arrangements to provide six feet of distance between students, which reduces the class size from 32 to 8 students; (b) presence and absence of computer monitors which provide some flow deflection; (c) increased occupancy of the classroom; (d) increased ventilation of six air changes per hour (ACH) compared to the recommended four ACH [56]; and (e) mask wearing by all versus some versus none of the occupants.

We can assess the transmission risk for the previously mentioned scenarios based on the flow field obtained from the CFD solutions of 3 different configurations. The first configuration (Configuration 1) represents a classroom setting in a lecture setup with 9 occupants (8 students and 1 lecturer) (Figure 8a). A seating plan is implemented in which the occupants are all located 3 to 6 feet apart from each other, as recommended by CDC guidelines. Configuration 1 serves as a benchmark for comparison with other configurations. The second scenario (Configuration 2) investigates 9 occupants (8 students and 1 lecturer) as well as 8 computers (Figure 8b). Configuration 2 aims to investigate the effect of computers on the flow field and, therefore, the risk of transmission. The last configuration (Configuration 3) examines 21 occupants (20 students and 1 lecturer) (Figure 8c). Configuration 3 depicts a high-risk scenario where the safe social distancing guidelines are compromised, and there are more occupants than recommended in an enclosed environment during an ongoing pandemic. This scenario aims to study the increase in transmission risk if basic social distancing guidelines are not followed.

For each of these configurations, we automatically create a well-refined mesh and perform combined heat and flow simulations to get the statistically steady flow field (see Section 2.2). Then, we consider a coughing event and perform passive scalar transport of virion concentration in the confined space. We perform this scalar transport for one full air change. Finally, we evaluate transmission risk by considering the inhaled viral load at various spatial locations in the room.

Our objective is to investigate the effects of face masks, the thermal plume caused by increased occupancy, and the thermal plume caused by electronics on the transport of virion particles within the classroom. Hence, we conducted a parameter study based on three different configurations.

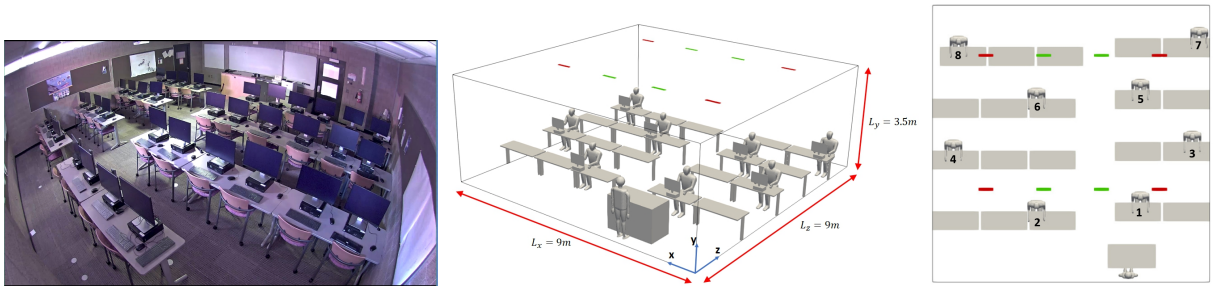

(a) *The actual classroom environment* **(b)** *Computational domain with computers* **(c)** *Vents and mannequin labels*

Figure 7: *Computational representation (b) of the enclosed space (a) to be used in the simulation. Top-down view of the classroom (c) with the inlet (green) and outlet (red) vents on the ceiling.*

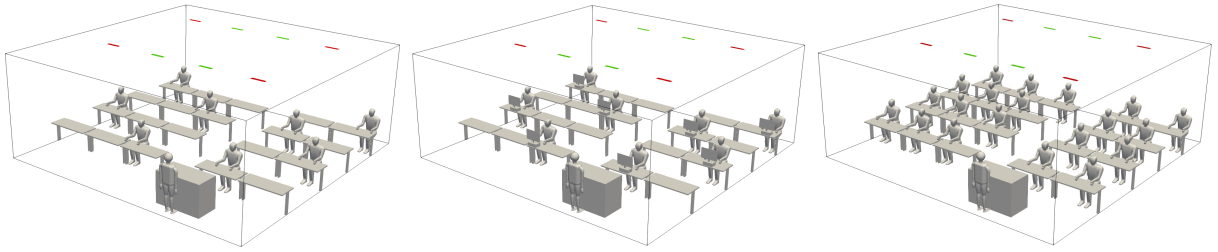

(a) *Configuration 1* **(b)** *Configuration 2* **(c)** *Configuration 3*

Figure 8: *Three different classroom layouts to be simulated.*

Figure 9: *Seating plan of the labeled mannequins.*

We investigated the three configurations by running simulations based on a simulated cough by one designated mannequin out of the eight seated mannequins in the classroom (Figure 9). The designated mannequin is varied in the simulations to study the effect of the coughers' location on the transmission risk within the classroom.

No-slip boundary conditions are applied to the walls and the surfaces of furniture, mannequins, and computers to solve the Navier-Stokes equations. A Dirichlet boundary condition of $U^* = 1$ is defined at the inlet vents to represent the speed of the jet leaving the vents into the classroom environment. A Dirichlet pressure boundary condition $P^* = 0$ is defined at the outlet vents. Dirichlet boundary conditions of 26.6°C on the surface of the mannequins, 21.3°C on the inlet vents, and 37.0°C on the surface of the computers are defined for the heat transfer equation. No heat flux boundary conditions are applied on the surfaces of the furniture and walls or the outlet vents of the classroom. No-flux boundary conditions are applied on the surfaces of the mannequins, furniture, and computers to solve the advection-diffusion transport of virion particles. The prescription of a no flux boundary condition in the AD solver for all surfaces implies a conservative approach which assumes that the virion particles do not land on or stick onto the surfaces of any bodies in the classroom and will always remain airborne. A Dirichlet boundary condition of $C^* = 0$ is defined at the inlet and outlet vents. This represents the supply of purified air into the classroom from the inlet vents, and a sink for the classroom air at the outlet vents.

4.1.2 Initial Conditions

The initial conditions of the air within the classroom are at rest with an ambient temperature of 21.3°C to obtain a statistically steady-state solution for the flow field from the solution of the Navier-Stokes and heat transfer equations. The initial condition of the viral load concentration is defined as zero everywhere in the computational domain of the classroom, except for the cone-shaped region in front of an arbitrarily chosen mannequin with a viral load concentration of $C^* = 1$. This cone-shaped region represents the initial region occupied by the virion particles released by a carrier shortly after a cough.

The temperature of the exhaled air is assumed to be that of the ambient room temperature at steady state. Since we are initializing the region occupied by the cough droplets when the exhaled air reaches an equilibrium with the ambient air, the temperature (and velocity) of the exhaled air is assumed to be the same as that of the ambient air. This occurs at approximately 0.4s after the exhalation process [47].

4.1.3 Mesh Setup

A carved-out and voxelized computational domain composed of an octree mesh represents the classroom with the mannequins, furniture, and electronics. An optimal grid size (Δ) that strikes a balance between the computational cost and accuracy of the simulation is determined from grid convergence studies, beginning with a grid size estimated by the Taylor microscale $\lambda = L_{ref}\sqrt{10}Re^{-\frac{1}{2}}$. Additional refinement is added to the region above the mannequins and the computers to compute the thermal plumes.

4.2 Simulation Results

Flow field within the classroom: The flow field within the classroom is primarily influenced by inflow from the inlet vents and the thermal plumes caused by the mannequins and computers. These heated bodies each generate a thermal plume that drives flow upward due to buoyancy. The plume reach is nearly the height of the classroom (3.5 m), and it creates localized vertical flow features toward the ceiling (Figure 10).

Figure 10d shows the streamlines along a vertical slice, the velocity magnitude of the thermal plume generated by a computer (0.6 $\mathrm{m/s}$) is found to be approximately twice that generated by a human (0.35 $\mathrm{m/s}$). When these plumes reach the ceiling, the flow moves along the ceiling plane, and part of this flow is recirculated back down when it hits the flow emanating from the inlet vents. This recirculation of air within the classroom due to the thermal plumes and inlet jets dilutes[3] the viral load concentration of the contaminated air within the enclosed space. The diluted viral load concentration is eventually removed from the classroom through the outlet vents.

Viral load concentration field: Upon the expulsion of viral-laden aerosols due to a coughing event, we find that the contaminated air eventually gets transported upward due to the thermal plume (see Figures in the Supplement). Following the streamlines, the viral load concentration field is recirculated due to the upward motion of the thermal plumes and the downward motion of the inlet flow. Successive recirculation further dilutes the viral load concentration until it is removed from the enclosed space via the outlet vents.

[3]This dilution of the aerosol concentration is caused by advection and diffusion due to the underlying flow field. A reminder that we do not consider drying, breakup or aggregation kinetics. See Section 5.

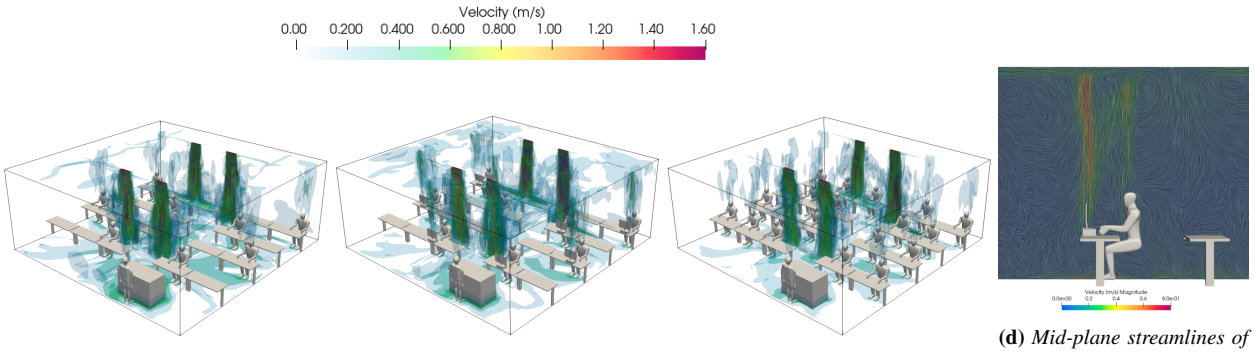

(a) *Configuration 1* **(b)** *Configuration 2* **(c)** *Configuration 3* **(d)** *Mid-plane streamlines of the flow around the objects*

Figure 10: *Visualization of the flow field field in a classroom for (a) Configuration 1: A classroom setting with 8 seated occupants and 1 standing occupant, (b) Configuration 2: A classroom setting with 8 seated occupants (each with a computer in front of them) and 1 standing occupant, (c) Configuration 3: A classroom setting with 20 seated occupants and 1 standing occupant and (d) streamlines representing the flow field around a mannequin and computer.*

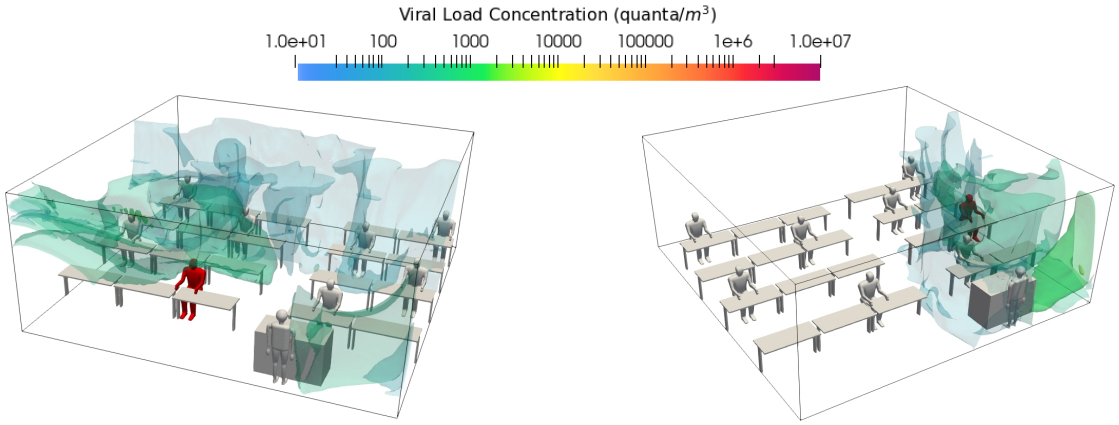

(a) *Simulated cough by mannequin 2*

(b) *Simulated cough by mannequin 3*

Figure 11: *Viral load concentration of the air 15 minutes after the simulated cough by the assigned mannequin (colored red).*

The temporal evolution of the viral load concentration field varies depending on location. We simulated coughing events at various positions and observed that the temporal evolution for locations that were not close to (and right below) the inlet vents were similar regardless of location. Therefore, we focus our transmission risk assessment on two canonical locations: a simulated cough by an infected individual seated directly beneath an inlet vent (mannequin 2, Figure 11a) and one seated away from the inlet vent (mannequin 3, Figure 11b). Please refer to Figure 9 for additional details and mannequin labels.

We observed that the virion-laden air dilutes (due to advection-diffusion) more rapidly when the cough occurs in the vicinity of an inlet vent (Figure 11a), and the viral concentration remains higher in a more localized region when the cough occurs further away from an inlet (Figure 11b). This is due to mixing of the contaminated air with the inlet jet, resulting in a lower viral load concentration at the end of an air change cycle when the cough occurs closer to an inlet. This higher rate of dilution suggests a potentially lower risk of transmission.

From these results, we also observe that the virion-laden air is transported over a long distance when released near the inlet vents; thus, the contaminated air can potentially occupy a larger volume of the classroom space than when released further away from the inlet vents (Figure 11). Hence, occupants more than 6 feet away from the infected individual may still be susceptible to infection if the total number of inhaled particles exceeds the minimum infective dose (MID). To assess the transmission risk under this complicated interaction, we consider these two competing outcomes, the viral load concentration of the contaminated air and the volume of space occupied by the contaminated air.

Transmission Risk Assessment

We can quantify the transmission risk assessment in terms of the total number of virion particles inhaled by an individual at any given position in the classroom throughout the simulation time (see Equation (34)). The transmission risk is quantified and visualized on a horizontal plane at breathing height for seated individuals (see Figure 3b). We quantify the transmission risk for the five specific scenarios mentioned earlier. For a better visualisation of the transmission risk contours, black and white contour lines are added to the contour plots to represent 50 and 100 inhaled virion particles respectively.

As a baseline, a localized region with a high transmission risk is observed in the region in front of mannequin 3 for a simulated cough event (in Configuration 1). However, this localized region only directly affects one other occupant (mannequin 1) (Figure 12f). Otherwise, the high transmission region is confined to a space in the classroom that is not occupied. The black contour lines demarcate the region within which

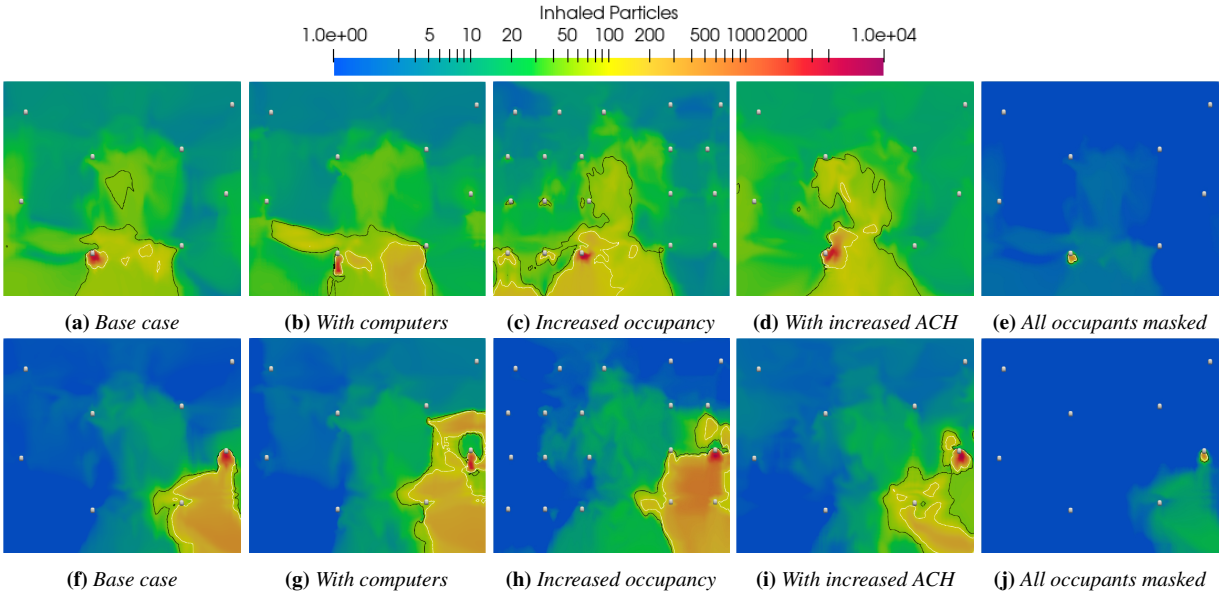

(a) *Base case* **(b)** *With computers* **(c)** *Increased occupancy* **(d)** *With increased ACH* **(e)** *All occupants masked*

(f) *Base case* **(g)** *With computers* **(h)** *Increased occupancy* **(i)** *With increased ACH* **(j)** *All occupants masked*

Figure 12: *Top view of each case with the contour of transmission risk shown at the end of one air change cycle due to a simulated cough by mannequin 2 (top row) and mannequin 3 (bottom row).*

50 or more virion particles will be inhaled ($N \geq 50$ based on Equation (34); see Methods section). These regions represent the space with a higher risk of infection. In contrast, we found that every seated occupant in the classroom experiences (at worst) a moderate risk of infection due to a simulated cough by mannequin 2 (Figure 12a). Note that mannequin 2 is seated underneath an inlet vent. Although fewer occupants are at risk of infection due to an infected mannequin 3 (Figure 12f), the affected individual would likely be more susceptible due to a higher count of inhaled virion particles than the exposure resulting from a cough by mannequin 2.

Impact of Electronics: When an infected individual coughs, we expect the physical presence of electronic equipment (such as a computer monitor) to block the virion-laden air from reaching other individuals. Furthermore, the thermal plume generated by the electronics may impede pathogen transmission by transporting the pathogen-laden aerosols upward away from the breathing zone of other individuals. Hence, intuitively, we expect the transmission risk to be reduced.

Surprisingly, the addition of computers does not dissipate the risk of transmission. In fact, it expands the localized region that has a high risk of transmission (Figure 12b, Figure 12g) based on the risk transmission assessment for Configuration 2. This phenomenon is observed for both cases of simulated cough by mannequin 2 and mannequin 3. The thermal plumes generated by the computers enhance the recirculation of the contaminated air and increase the region with higher transmission risk (Figure 10). In Configuration 2 (with reduced occupancy), the expanded region with high transmission risk does not further implicate any previously unaffected occupants since it is confined to a region of space that is unoccupied (Figure 12g). However, mannequin 1 will experience a greater risk of infection caused by a cough by mannequin 2.

Impact of Increased Occupancy: Increased occupancy within an enclosed space decreases the proximity between individuals to ≈ 3 feet and increases the ease of transmission of virion particles. It also introduces additional thermal plumes that alter the flow field of the classroom, complicating the risk assessment.

Based on the risk assessment conducted for Configuration 3, which represents a classroom setting with an occupancy of 20 students (Figure 8c), we find that the region of transmission risk increases with occupancy (Figure 12c, Figure 12h). In adherence to social distancing guidelines, a decrease in the occupancy of the

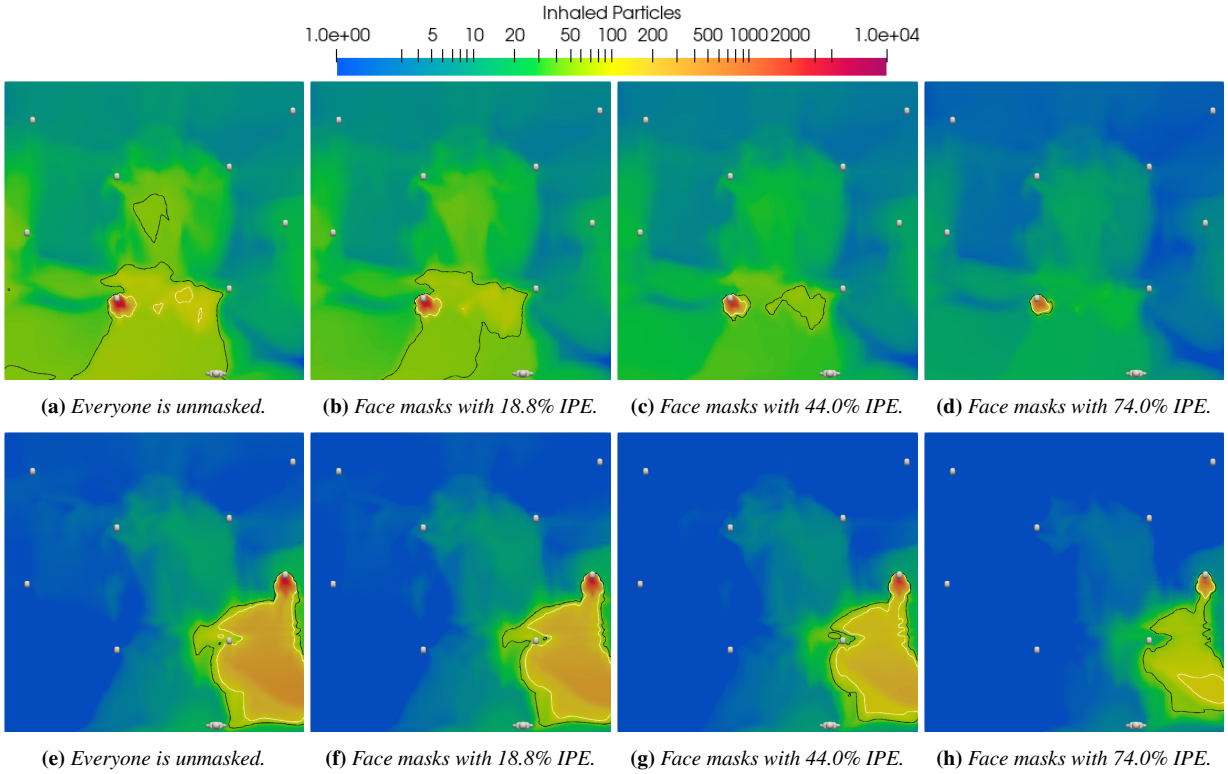

(a) *Everyone is unmasked.* **(b)** *Face masks with 18.8% IPE.* **(c)** *Face masks with 44.0% IPE.* **(d)** *Face masks with 74.0% IPE.*

(e) *Everyone is unmasked.* **(f)** *Face masks with 18.8% IPE.* **(g)** *Face masks with 44.0% IPE.* **(h)** *Face masks with 74.0% IPE.*

Figure 13: *Comparison of the amount of protection each type of face masks provide users with against a simulated cough by unmasked mannequin 2 (top row) and mannequin 3 (bottom row).*

classroom (from a class size of 20 in Configuration 3 to 8 in Configuration 2) decreases the risk slightly by increasing the distance the virion particles have to travel from their source (the infected cougher). However, social distancing guidelines still do not provide the occupants with sufficient protection against an infection risk in the presence of computers that redirect the flow, as shown in (Figure 12b, Figure 12g).

Impact of Increased Air Changes: An increase in air changes per hour (ACH) for an enclosed space will increase the volume of purified air entering the classroom. We examined the effect of increased ACH on the transmission risk by increasing the ACH from 4 to 6 for Configuration 1. In this case, we notice rapid dilution of the contaminated air due to a simulated cough at the higher ACH. The higher ventilation with increased ACH reduces the size of the localized regions of transmission risk (Figure 12d, Figure 12i).

Impact of Face Mask Usage: The use of face masks significantly reduces the viral load released by an infected individual during exhalation compared to other mitigation strategies. The flow resistance of face masks impedes the spread of the cough cloud from the individual. Hence, the cough cloud released by a masked individual differs in size and viral load density from an unmasked individual.

The impact of face masks on risk transmission is evaluated based on the classroom setting described in Configuration 1. In this configuration, all of the occupants are assumed to be wearing surgical masks. The surgical mask is capable of preventing 94% of the virion aerosols from being released by a masked cougher [49], and it decreases the extent of the respective cough cloud to 35 cm (from 70 cm for a maskless cough) due to its flow resistance [24]. The inward protection efficiency (IPE) of the surgical mask worn by all occupants is assumed to be 18.81% [57]. This implies that the masked occupants inhale at most 81.19% of the virion-laden aerosols from the ambient air.

The use of face masks tremendously reduces the transmission risks such that no occupants have inhaled a significant quantity of virion particles (Figure 12e, Figure 12j) as compared to the case where a majority of the occupants in the class are at moderate risk of becoming infected because everyone is unmasked (Figure 12a, Figure 12f). Furthermore, the extent of the region of transmission risk is significantly reduced and confined to the space in front of the cougher's mouth. Thus, everyone wearing masks (even sub-optimally, as evidenced by the 18.8% inward protection efficiency) produces the most significant risk reduction.

While the transmission risk is minimal when every occupant is masked, this might not be the most prevalent scenario with the relaxation of the mask mandates. An unmasked asymptomatic carrier may endanger other individuals nearby, making them susceptible to infection. Hence, we investigate the protection offered by face masks to a masked individual from other unmasked and infected individuals.

Due to the gap between the face mask and the face, the IPE of the masks is significantly lower than the material filtration efficiency. The IPE of current existing surgical masks ranges from 18.8%[57] to 44.0% [58], to even 74%. We next evaluate the impact on various IPE on risk profiles as shown in Figure 13. Most face masks provide users with sufficient protection against a cough by an unmasked mannequin 2. However, mannequin 1 would still be susceptible to an infection due to cough by an unmasked mannequin 3 with the use of existing face masks with IPE between 18.8% to 44.0%. This suggests a need to improve the mask design to get a better IPE that provides users with better protection against other unmasked individuals.

Researchers have been proposing improved mask designs (as well as methods to achieve a snug fit) that result in higher IPE and can provide users with sufficient protection against an airborne transmission. Pan et al. [59] have proposed an improved three-layer mask design that provides users with at least 74% IPE. The effectiveness of the improved face mask design is tested in our simulations with the results shown in Figure 13d and Figure 13h. These masks provide users with sufficient protection against other unmasked individuals. In most cases, with a high-efficiency mask, when worn correctly, the transmission risk to masked individuals is very low, even if the infected individual chooses to be unmasked (see additional data in the Supplement).

4.3 Additional Quantitative Analysis

Based on the results presented in the previous section, it is observed that mannequin 1 is usually affected by a cough by mannequins 2 and 3 under various settings. We can further quantify the risk of transmission at discrete inhalation points between these mannequins. We considered two directions to compute this risk – one from mannequin 2 to 1, and another from mannequin 3 to 1, as shown in Figure 14. We note this is

Figure 14: *Direction of the line from mannequin 2 to 1 (left) and from mannequin 3 to 1 (right) along which the number of inhaled particles will be plotted against the arc length.*

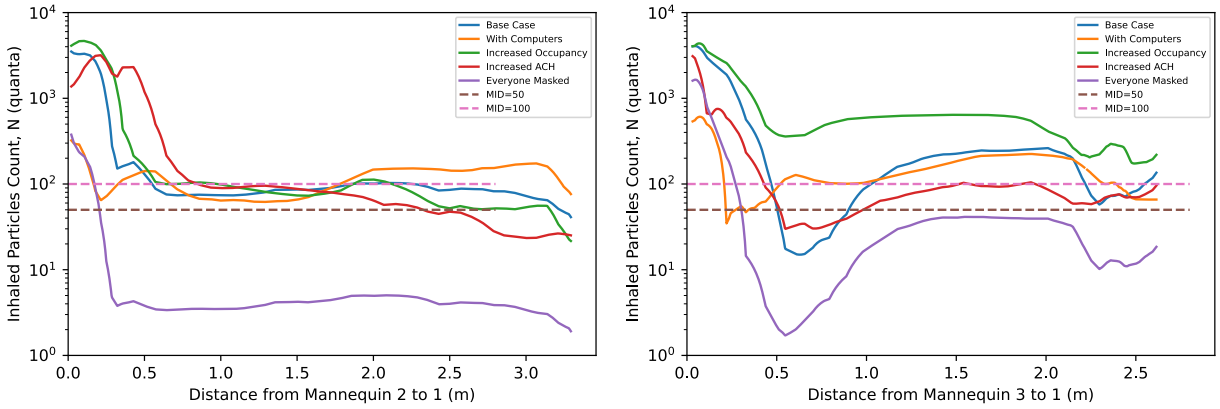

(a) *Plot along a line due to a cough by mannequin 2.*

(b) *Plot along a line due to a cough by mannequin 3.*

Figure 15: *Plot of number of inhaled particles along a line from mannequin 2 to 1 (left) and from 3 to 1 (right).*

essentially a line cut of the figures plotted in the earlier section. Figure 15 plots the inhaled particles along these two line cuts for all the scenarios considered. It is observed that precautionary measures, such as a reduction in the occupancy and increasing the ventilation rate, decrease the transmission risk by approximately 2 times due to cough by Mannequin 3 (Figure 15b). However, such precautionary measures would not be effective if the infected individual is seated near a vent. This can be observed based on how relatively indifferent the transmission risk is due to the different settings (Figure 15a).

It is also found that mandating all occupants to use face masks is effective in decreasing the risk of transmission by at least 10 times regardless of where the infected individual is located at. Furthermore, mandating everyone to wear face masks actually ensures that the transmission risk is always lower than the MID at beyond 0.3m away from the infected individual.

5 Discussion and Conclusions

Our results show that localized regions of high risk of transmission can exist in a classroom (and more generally indoor environments) even when occupants are well spaced apart and ventilation rates are increased. However, the risk of transmission is significantly reduced if the infected individual is masked. Even when an infected individual chooses to remain unmasked, proper masking–that ensures moderate infiltration efficiency (or inward protection efficiency)–by other individuals reduces the risk of transmission to them.

We next discuss simplifying assumptions made and their implications on our results.

- Distribution of initial cough cloud: A coughing event is initialized as a cough cloud represented by a cone-shaped region of homogeneously distributed virion concentration in front of the cougher's mouth. A small number of virion particles that lie outside the cough cloud are neglected (Figure 3a). Extending the cone-shaped region does not significantly change any of the results.
- Distribution of initial cough cloud under masked conditions: The viral shedding from leakages along the edges of the mask is neglected in the initialization of the cough droplets released by a masked cougher. A more accurate initial condition for the virion particles can improve the representation of the location of discrete virion particles outside of the cough cloud and in the leakage regions along the edges of the face mask. As before, slight changes to the initial cough cloud do not significantly change any of the conclusions.

- Scalar transport of virion particle density: We only consider particles of size less than $10\mu\mathrm{m}$. We only consider the advective and diffusive transport of the virion particles (Equation 11). This equation does not account for the depletion of the viral load density in the contaminated air, perhaps due to the deactivation of the virus, depletion of virion particles when inhaled by the occupants, and the adhesion of virion particles to contacted surfaces. We also do not consider the impact of humidity on the distribution. In this context, our results can be considered conservative estimates of the transmission risk since relaxing these assumptions will reduce the virion concentration field and transmission risk.
- Particle-particle interactions: Our simulation framework–specifically the advection-diffusion equation that models the concentration evolution–does not account for drying, aggregation, or break-up of the particles. We consider particles with diameters $\leq 10\mu m$, which do not generally undergo break-up. Thus, without drying, our simulations represent a conservative estimate of the transport risk of aerosolized particles. Moreover, our framework naturally allows the extension to model aggregation, break-up, and drying by considering the population balance equations. This is the focus of future work.
- An assumption involved with the transmission risk assessment is that the viral load density remains relatively unchanged when inhaled by the occupants. This assumption is commonly adopted across the literature [7–9].

We illustrate a computational approach that can automatically and efficiently evaluate transmission risk in geometrically complex indoor settings. This approach abstracts away the complexity of mesh generation and subsequent simulation and analysis, thus allowing straightforward deployment by end-users. Our use of a LES type model (rather than RANS models) further removes any scenario specific model fine-tuning that an end-user needs to perform. Furthermore, the ubiquity of cloud computing resources can allow democratization of such simulation tools [60]. The availability of such a personalized planning tool will enable educational institutions (K-12, community colleges, universities) and other entities (courthouses, public transport locations, hospitals) to evaluate various in-person interaction scenarios comprehensively. Such a framework will help quantify and minimize the risk of infection. We illustrate the utility of the framework by evaluating risk for different seating, ventilation, and mask-wearing scenarios in a canonical classroom. Wearing masks significantly reduces the risk of transmission of the SARS-CoV-2 virus. More broadly, this framework for personalized transmission risk assessment may also be applied to other airborne transmittable pathogens based on the known information about the pathogen and its minimum infection dosage (MID) and can be useful in other critical care infrastructures such as hospitals (operation theaters, infectious wards, etc.). This work is a step in the path to democratization of complex simulation software to the broader scientific and application community.

Conflict of Interest Statement

The authors have no competing interests to declare that are relevant to the content of this article.

Acknowledgements

This work was partly supported by the National Science Foundation under grant number OAC 1750865, MRI 2018594, CBET 1935255, CMMI 2053760. MCH was partially supported by NIH/NHLBI Award No. R01HL142504. Computing resources were supported by Frontera Pathways allocation PHY20033.

References

[1] Centers for Disease Control (CDC). How COVID-19 spreads, 2020. URL https://www.cdc.gov/coronavirus/2019-ncov/prevent-getting-sick/how-covid-spreads.html.

[2] World Heath Organization (WHO). Advice for the public on COVID-19, 2021. URL https://www.who.int/emergencies/diseases/novel-coronavirus-2019/advice-for-public.

[3] Lea Hamner. High SARS-CoV-2 attack rate following exposure at a choir practice–skagit county, washington, march 2020. *MMWR. Morbidity and mortality weekly report*, 69, 2020.

[4] Shelly L. Miller, William W. Nazaroff, Jose L. Jimenez, Atze Boerstra, Giorgio Buonanno, Stephanie J. Dancer, Jarek Kurnitski, Linsey C. Marr, Lidia Morawska, and Catherine Noakes. Transmission of SARS-CoV-2 by inhalation of respiratory aerosol in the skagit valley chorale superspreading event. *Indoor air*, 31(2):314–323, 2021.

[5] Neeltje van Doremalen, Trenton Bushmaker, Dylan H. Morris, Myndi G. Holbrook, Amandine Gamble, Brandi N. Williamson, Azaibi Tamin, Jennifer L. Harcourt, Natalie J. Thornburg, Susan I. Gerber, and et al. Aerosol and surface stability of SARS-CoV-2 as compared with sars-cov-1. *New England Journal of Medicine*, 382(16):1564–1567, 2020. doi: 10.1056/nejmc2004973.

[6] Nan Zhang, Xuguang Chen, Wei Jia, Tianyi Jin, Shenglan Xiao, Wenzhao Chen, Jian Hang, Cuiyun Ou, Hao Lei, Hua Qian, et al. Evidence for lack of transmission by close contact and surface touch in a restaurant outbreak of COVID-19. *Journal of Infection*, 2021.

[7] Siyao Shao, Dezhi Zhou, Ruichen He, Jiaqi Li, Shufan Zou, Kevin Mallery, Santosh Kumar, Suo Yang, and Jiarong Hong. Risk assessment of airborne transmission of COVID-19 by asymptomatic individuals under different practical settings. *Journal of Aerosol Science*, 151:105661, 2021. ISSN 0021-8502. doi: 10.1016/j.jaerosci.2020.105661. URL https://www.sciencedirect.com/science/article/pii/S0021850220301476.

[8] Ville Vuorinen, Mia Aarnio, Mikko Alava, Ville Alopaeus, Nina Atanasova, Mikko Auvinen, Nallannan Balasubramanian, Hadi Bordbar, Panu Erästö, Rafael Grande, and et al. Modelling aerosol transport and virus exposure with numerical simulations in relation to SARS-CoV-2 transmission by inhalation indoors. *Safety Science*, 130:104866, 2020. doi: 10.1016/j.ssci.2020.104866.

[9] Zhihang Zhang, Taehoon Han, Hee Yoo Kwang, Jesse Capecelatro, André L. Boehman, and Kevin Maki. Disease transmission through expiratory aerosols on an urban bus. *Physics of Fluids*, 33(1), 2021. doi: 10.1063/5.0037452.

[10] Lydia Bourouiba, Eline Dehandschoewercker, and John W. M. Bush. Violent expiratory events: on coughing and sneezing. *Journal of Fluid Mechanics*, 745:537–563, 2014. doi: 10.1017/jfm.2014.88.

[11] Lydia Bourouiba. The fluid dynamics of disease transmission. *Annual Review of Fluid Mechanics*, 53 (1):473–508, 2021. doi: 10.1146/annurev-fluid-060220-113712.

[12] Siddhartha Verma, Manhar Dhanak, and John Frankenfield. Visualizing the effectiveness of face masks in obstructing respiratory jets. *Physics of Fluids*, 32(6):061708, June 2020. doi: 10.1063/5.0016018.

[13] Rajat Mittal, Rui Ni, and Jung-Hee Seo. The flow physics of COVID-19. *Journal of Fluid Mechanics*, 894:F2, 2020. doi: 10.1017/jfm.2020.330.

[14] J. W. Tang, W. P. Bahnfleth, P. M. Bluyssen, G. Buonanno, J. L. Jimenez, J. Kurnitski, Y. Li, S. Miller, C. Sekhar, and L. Morawska. Dismantling myths on the airborne transmission of severe acute respiratory syndrome coronavirus-2 (SARS-CoV-2). *Journal of Hospital Infection*, 110:89–96, 2021. doi: 10.1016/j.jhin.2020.12.022.

[15] C. Y. H. Chao, M. P. Wan, L. Morawska, G. R. Johnson, Z. D. Ristovski, M. Hargreaves, K. Mengersen, S. Corbett, Y. Li, X. Xie, and D. Katoshevski. Characterization of expiration air jets and droplet size distributions immediately at the mouth opening. *Journal of Aerosol Science*, 40(2):122–133, 2009. ISSN 0021-8502. doi: 10.1016/j.jaerosci.2008.10.003. URL https://www.sciencedirect.com/science/article/pii/S0021850208001882.

[16] Mark Nicas, William W. Nazaroff, and Alan Hubbard. Toward understanding the risk of secondary airborne infection: emission of respirable pathogens. *Journal of Occupational and Environmental Hygiene*, 2(3):143–154, March 2005. doi: 10.1080/15459620590918466.

[17] Jeffrey Slotnick, Abdollah Khodadoust, Juan Alonso, David Darmofal, William Gropp, Elizabeth Lurie, and Dimitri Mavriplis. CFD vision 2030 study: A path to revolutionary computational aerosciences, 2014.

[18] F. Xu, D. Schillinger, D. Kamensky, V. Varduhn, C. Wang, and M.-C. Hsu. The tetrahedral finite cell method for fluids: Immersogeometric analysis of turbulent flow around complex geometries. *Computers & Fluids*, 141:135–154, 2016.

[19] Kumar Saurabh, Masado Ishii, Milinda Fernando, Boshun Gao, Kendrick Tan, Ming-Chen Hsu, Adarsh Krishnamurthy, Hari Sundar, and Baskar Ganapathysubramanian. Scalable adaptive pde solvers in arbitrary domains. In *Proceedings of the International Conference for High Performance Computing, Networking, Storage and Analysis*, pages 1–15, 2021.

[20] Kumar Saurabh, Boshun Gao, Milinda Fernando, Songzhe Xu, Makrand A. Khanwale, Biswajit Khara, Ming-Chen Hsu, Adarsh Krishnamurthy, Hari Sundar, and Baskar Ganapathysubramanian. Industrial scale Large Eddy Simulations with adaptive octree meshes using immersogeometric analysis. *Computers & Mathematics with Applications*, 97:28–44, 2021.

[21] Songzhe Xu, Boshun Gao, Ming-Chen Hsu, and Baskar Ganapathysubramanian. A residual-based variational multiscale method with weak imposition of boundary conditions for buoyancy-driven flows. *Computer Methods in Applied Mechanics and Engineering*, 352:345–368, 2019.

[22] Y. Bazilevs, V. M. Calo, J. A. Cottrell, T. J. R. Hughes, A. Reali, and G. Scovazzi. Variational multiscale residual-based turbulence modeling for large eddy simulation of incompressible flows. *Computer Methods in Applied Mechanics and Engineering*, 197:173–201, 2007.

[23] John M. Kolinski and Tobias M. Schneider. Superspreading events suggest aerosol transmission of SARS-CoV-2 by accumulation in enclosed spaces. *Phys. Rev. E*, 103(3):033109, 2021. doi: 10.1103/PhysRevE.103.033109.

[24] Talib Dbouk and Dimitris Drikakis. On respiratory droplets and face masks. *Physics of Fluids*, 32(6), 2020. doi: 10.1063/5.0015044.

[25] Dongjie Jia, Jonathan Lee Baker, Anaïs Rameau, and Mahdi Esmaily. Simulation of a vacuum helmet to contain pathogen-bearing droplets in dental and otolaryngologic outpatient interventions. *Physics of Fluids*, 33(1):013307, 2021. doi: 10.1063/5.0036749.

[26] Sai Ranjeet Narayanan and Suo Yang. Airborne transmission of virus-laden aerosols inside a music

classroom: effects of portable purifiers and aerosol injection rates. *Physics of Fluids*, 33(3):033307, 2021. doi: 10.1063/5.0042474.

[27] Hongying Li, Fong Yew Leong, George Xu, Zhengwei Ge, Chang Wei Kang, and Keng Hui Lim. Dispersion of evaporating cough droplets in tropical outdoor environment. *Physics of Fluids*, 32(11): 113301, 2020. doi: 10.1063/5.0026360.

[28] Vladimir P. Zhdanov and Bengt Kasemo. Virions and respiratory droplets in air: diffusion, drift, and contact with the epithelium. *Biosystems*, 198:104241, 2020. ISSN 0303-2647. doi: 10.1016/j.biosystems.2020.104241. URL https://www.sciencedirect.com/science/article/pii/S0303264720301295.

[29] Kristen K. Coleman, Douglas Jie Wen Tay, Kai Sen Tan, Sean Wei Xiang Ong, Ming Hui Koh, Yi Qing Chin, Haziq Nasir, Tze Minn Mak, Justin Jang Hann Chu, Donald K. Milton, et al. Viral load of SARS-CoV-2 in respiratory aerosols emitted by COVID-19 patients while breathing, talking, and singing. *medRxiv*, 2021.

[30] Mohamed Abuhegazy, Khaled Talaat, Osman Anderoglu, and Svetlana V. Poroseva. Numerical investigation of aerosol transport in a classroom with relevance to COVID-19. *Physics of Fluids*, 32(10): 103311, 2020.

[31] J. P. Duguid. The size and the duration of air-carriage of respiratory droplets and droplet-nuclei. *Epidemiology and Infection*, 44(6):471–479, 1946. doi: 10.1017/s0022172400019288.

[32] L. Morawska, G. R. Johnson, Z. D. Ristovski, M. Hargreaves, K. Mengersen, S. Corbett, C. Y. H. Chao, Y. Li, and D. Katoshevski. Size distribution and sites of origin of droplets expelled from the human respiratory tract during expiratory activities. *Journal of Aerosol Science*, 40(3):256–269, 2009. ISSN 0021-8502. doi: 10.1016/j.jaerosci.2008.11.002. URL https://www.sciencedirect.com/science/article/pii/S0021850208002036.

[33] Xiaojian Xie, Yuguo Li, Hequan Sun, and Li Liu. Exhaled droplets due to talking and coughing. *Journal of The Royal Society Interface*, 6, 2009. doi: 10.1098/rsif.2009.0388.focus.

[34] Shinhao Yang, Grace Lee, Cheng-Min Chen, Chih-Cheng Wu, and Kuo-Pin Yu. The size and concentration of droplets generated by coughing in human subjects. *Journal of Aerosol Medicine*, 20(4): 484–494, 2007. doi: 10.1089/jam.2007.0610.

[35] G. R. Johnson, L. Morawska, Z. D. Ristovski, M. Hargreaves, K. Mengersen, C. Y. H. Chao, M. P. Wan, Y. Li, X. Xie, D. Katoshevski, and S. Corbett. Modality of human expired aerosol size distributions. *Journal of Aerosol Science*, 42(12):839–851, 2011. ISSN 0021-8502. doi: 10.1016/j.jaerosci.2011.07.009. URL https://www.sciencedirect.com/science/article/pii/S0021850211001200.

[36] William G. Lindsley, Terri A. Pearce, Judith B. Hudnall, Kristina A. Davis, Stephen M. Davis, Melanie A. Fisher, Rashida Khakoo, Jan E. Palmer, Karen E. Clark, Ismail Celik, et al. Quantity and size distribution of cough-generated aerosol particles produced by influenza patients during and after illness. *Journal of occupational and environmental hygiene*, 9(7):443–449, 2012.

[37] Yongjie Jessica Zhang. *Geometric modeling and mesh generation from scanned images*. CRC Press, Boca Raton, 2016.

[38] Marshall Bern and Paul Plassmann. Mesh generation. *Handbook of Computational Geometry*, pages 291–332, 2000. doi: 10.1016/b978-044482537-7/50007-3.

[39] Michael J. Aftosmis. Solution adaptive Cartesian grid methods for aerodynamic flows with complex geometries. *von Karman Institute for Fluid Dynamics Computational Fluid Dynamics Lecture Series*, 1997.

[40] Martin Z. Bazant and John W. Bush. A guideline to limit indoor airborne transmission of covid-19. *Proceedings of the National Academy of Sciences*, 118(17), 2021. doi: 10.1073/pnas.2018995118.

[41] M. Elizabeth Halloran, Ira M. Longini, and Claudio Struchiner. Design and analysis of vaccine studies. *Statistics for Biology and Health*, 2010. doi: 10.1007/978-0-387-68636-3.

[42] Naiping Gao, Jianlei Niu, and Lidia Morawska. Distribution of respiratory droplets in enclosed environments under different air distribution methods. *Building Simulation*, 1(4):326–335, 2008. doi: 10.1007/s12273-008-8328-0.

[43] Alexander N. Brooks and Thomas J. R. Hughes. Streamline upwind Petrov-Galerkin formulations for convection dominated flow with particular emphasis on the incompressible Navier-Stokes equations. *Computer Methods in Applied Mechanics and Engineering*, 32(1-3):199–259, 1982. doi: 10.1016/0045-7825(82)90071-8.

[44] T. E. Tezduyar, S. Mittal, S. E. Ray, and R. Shih. Incompressible flow computations with stabilized bilinear and linear equal-order-interpolation velocity-pressure elements. *Computer Methods in Applied Mechanics and Engineering*, 95(2):221–242, 1992. doi: 10.1016/0045-7825(92)90141-6.

[45] Susanne C. Brenner and L. Ridgway Scott. *The mathematical theory of finite element methods*. Springer, 2007.

[46] Claes Johnson. *Numerical solution of partial differential equations by the finite element method*. Dover, 2009.

[47] Alexandre Fabregat, Ferran Gisbert, Anton Vernet, Som Dutta, Ketan Mittal, and Jordi Pallarès. Direct numerical simulation of the turbulent flow generated during a violent expiratory event. *Physics of Fluids*, 33(3):035122, 2021.

[48] Yang Wang, Guang Xu, and Yue-Wern Huang. Modeling the load of SARS-CoV-2 virus in human expelled particles during coughing and speaking. *PLOS ONE*, 15(10), 2020. doi: 10.1371/journal.pone.0241539.

[49] Liqiao Li, Muchuan Niu, and Yifang Zhu. Assessing the effectiveness of using various face coverings to mitigate the transport of airborne particles produced by coughing indoors. *Aerosol Science and Technology*, 55(3):332–339, 2020. doi: 10.1080/02786826.2020.1846679.

[50] Christian J. Kähler and Rainer Hain. Fundamental protective mechanisms of face masks against droplet infections. *Journal of Aerosol Science*, 148:105617, 2020. ISSN 0021-8502. doi: 10.1016/j.jaerosci.2020.105617. URL https://www.sciencedirect.com/science/article/pii/S0021850220301063.

[51] Sasha Hallett. Physiology, Tidal volume, 2020. URL https://www.ncbi.nlm.nih.gov/books/NBK482502/.

[52] Kim E. Barrett, Susan M. Barman, Scott Boitano, and Heddwen L. Brooks. *Ganong's review of medical physiology*. McGraw-Hill, 2013.

[53] Stuart W. Churchill. Free convection around immersed bodies. *Heat Exchanger Design Handbook*, 2, 2002.

[54] Stephen Whitaker. Forced convection heat transfer correlations for flow in pipes, past flat plates, single cylinders, single spheres, and for flow in packed beds and tube bundles. *AIChE Journal*, 18(2):361–371, March 1972. doi: 10.1002/aic.690180219.

[55] Brent A. Craven and Gary S. Settles. A computational and experimental investigation of the human thermal plume. *Journal of Fluids Engineering*, 128(6):1251–1258, 2006. ISSN 0098-2202. doi: 10.1115/1.2353274.

[56] Joseph G. Allen and Andrew M. Ibrahim. Indoor air changes and potential implications for SARS-CoV-2 transmission. *JAMA*, 325(20):2112, 2021. doi: 10.1001/jama.2021.5053.

[57] Mervin Zhao, Lei Liao, Wang Xiao, Xuanze Yu, Haotian Wang, Qiqi Wang, Ying Ling Lin, F. Selcen Kilinc-Balci, Amy Price, Larry Chu, and et al. Household materials selection for homemade cloth face coverings and their filtration efficiency enhancement with triboelectric charging. *Nano Letters*, 20(7): 5544–5552, 2020. doi: 10.1021/acs.nanolett.0c02211.

[58] Abhiteja Konda, Abhinav Prakash, Gregory A. Moss, Michael Schmoldt, Gregory D. Grant, and Supratik Guha. Aerosol filtration efficiency of common fabrics used in respiratory cloth masks. *ACS nano*, 14(5):6339–6347, 2020.

[59] Jin Pan, Charbel Harb, Weinan Leng, and Linsey C. Marr. Inward and outward effectiveness of cloth masks, a surgical mask, and a face shield. *Aerosol Science and Technology*, 55(6):718–733, 2021. doi: 10.1080/02786826.2021.1890687.

[60] Kumar Saurabh, Santi Adavani, Kendrick Tan, Masado Ishii, Boshun Gao, Adarsh Krishnamurthy, Hari Sundar, and Baskar Ganapathysubramanian. Case study of SARS-CoV-2 transmission risk assessment in indoor environments using cloud computing resources. *arXiv preprint arXiv:2111.09353*, 2021. Proceedings of SuperCompCloud: 5th Workshop on Interoperability of Supercomputing and Cloud Technologies.

SUPPLEMENT

We present some additional results of our simulations supporting our conclusions here.

A Concentration of Viral Load Over Time

A thermal plume is induced due to the buoyancy effect created by the temperature difference between the mannequin and the cooler ambient air. The thermal plume directs a flow upwards with a relatively high velocity before it gets redistributed in the lateral directions with a lower speed upon hitting the ceiling as observed in Figure 10. Hence, the initial transport of the virion-laden air is relatively rapid when they are first exhaled by the mannequin. Upon reaching the ceiling, the rate of transport and dilution of the contaminated air began to slow down, as shown in Figure A.1. As compared to the cough by mannequin 3, the contaminated air due to cough by mannequin 2 experiences a higher rate of transport and dilution as shown in Figure A.2. This increased transport rate is due to the jet of purified air directed towards mannequin 2 from the ceiling, which contributes to an increased advective transport and dilution of the contaminated air.

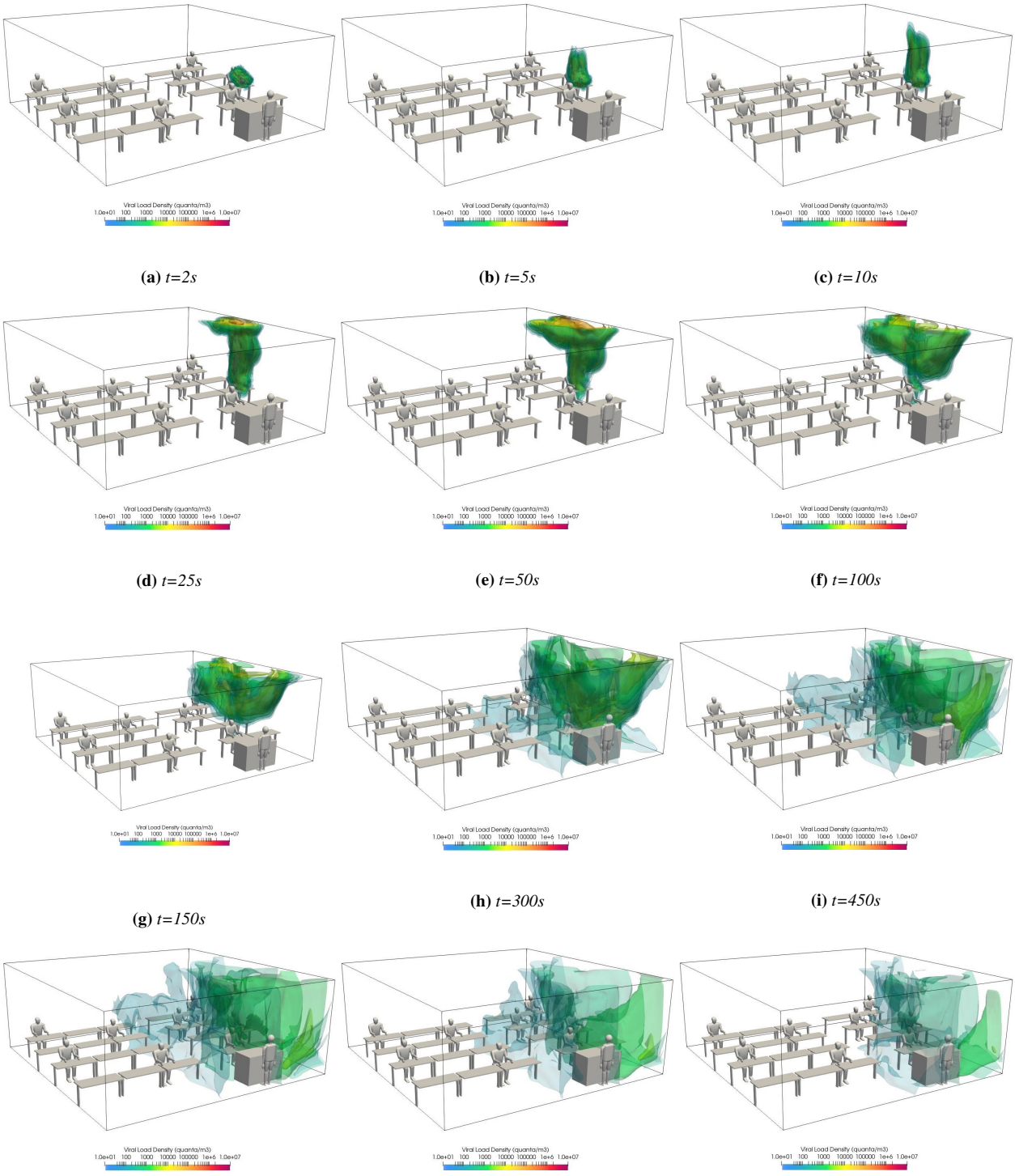

(a) *t=2s* **(b)** *t=5s* **(c)** *t=10s*

(d) *t=25s* **(e)** *t=50s* **(f)** *t=100s*

(g) *t=150s* **(h)** *t=300s* **(i)** *t=450s*

(j) *t=600s* **(k)** *t=750s* **(l)** *t=900s*

Figure A.1: *Time evolution of the viral load concentration of the air due to a simulated cough by Mannequin 3.*

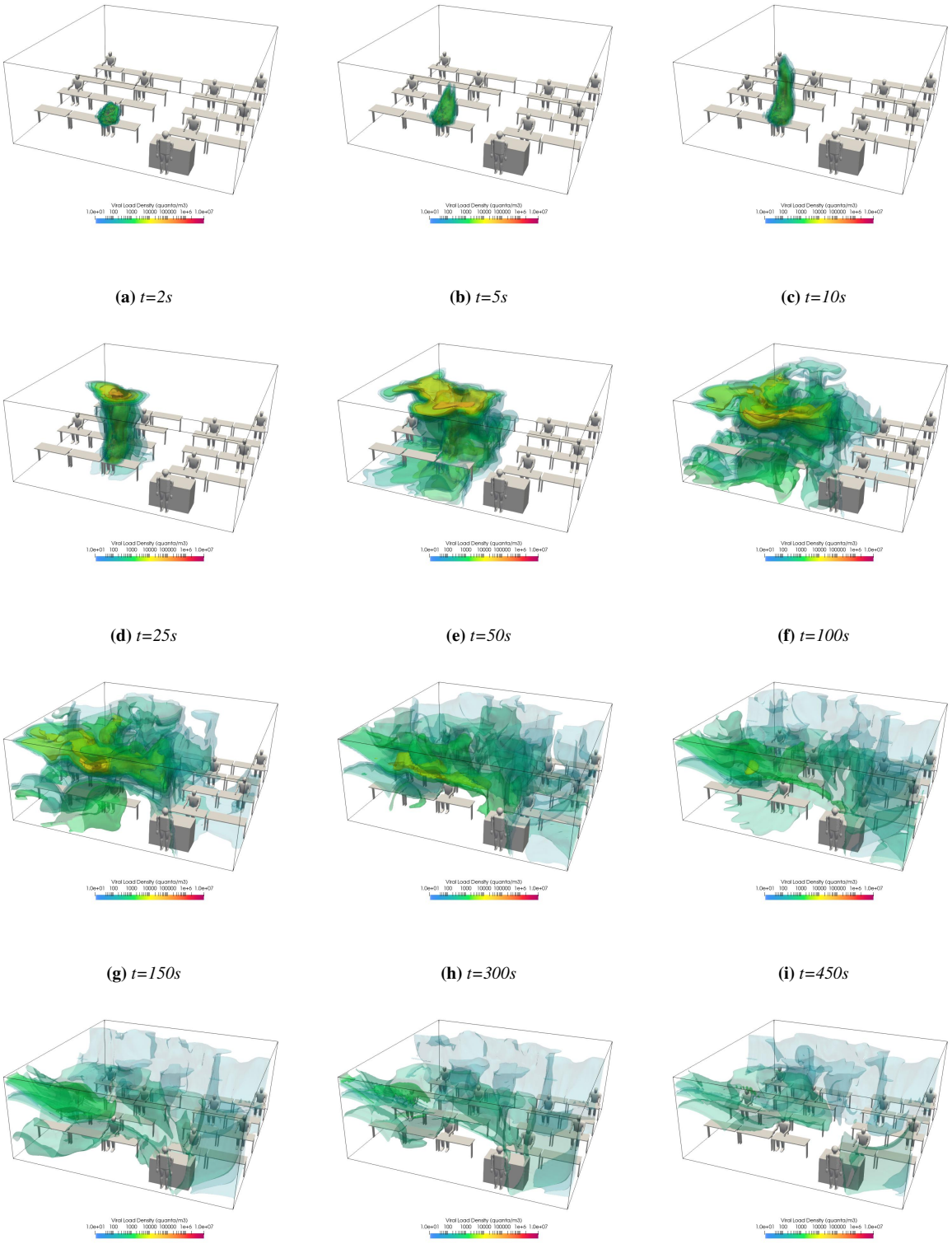

(a) *t=2s* **(b)** *t=5s* **(c)** *t=10s*

(d) *t=25s* **(e)** *t=50s* **(f)** *t=100s*

(g) *t=150s* **(h)** *t=300s* **(i)** *t=450s*

(j) *t=600s* **(k)** *t=750s* **(l)** *t=900s*

Figure A.2: *Time evolution of the viral load concentration of the air due to a simulated cough by Mannequin 2.*

B Transmission Risk Contours

B.1 Efficacy of Masks

In general, it is found that a cough released by the mannequins that are located away from the inlet vents will result in a smaller region of transmission risk (Figure A.3). However, these regions of transmission risk are observed to be localized with a higher risk of transmission than those generated by mannequins located closer to the inlet vents. This is due to the lack of advective transport of the virion particles. Hence, a higher concentration of virion particles lingers in the regions near the coughing mannequins for a relatively long period, contributing to the localized regions with a higher risk of transmission.

The use of surgical masks provides users and the individuals around them with inward and outward protection. The outward protection entails the filtration and reduction of the virion-laden aerosols exhaled by an infected mask user. On the other hand, inward protection involves the filtration of the virion-laden aerosols inhaled by the mask users from the ambient contaminated air. The outward protection efficiency (OPE) determines the proportion of the virion particles that an infected mask user can exhale. In contrast, the inward protection efficiency (IPE) determines the proportion of the virion particles inhaled by the mask user from the ambient contaminated air.

Ideally, the OPE and IPE should match the material filtration efficiency (MFE). However, due to different degrees of fit (due to the varying mask designs and material properties) and the environment that the masks are worn under, the OPE and IPE are lower than the MPE of the face mask [1]. Multiple works of literature reported similar OPE but varying IPE for surgical masks. The IPE reported for a typical surgical mask (with loose-fitting and the user's facial structure accounted for) may be as low as 18.81% [2].

With the relaxing of the mask mandate, there is a higher tendency for individuals to be unmasked. An infected individual releases about 16.7 times more airborne virion particles when unmasked [3], and there is a higher risk of transmission to the individuals nearby. In such situations, the susceptible individuals should use personal protective equipment (such as a face mask or shield) to protect themselves against the inhalation of the virion-laden aerosols released by the infected individuals. However, we found that typical surgical masks (with an inward protection efficiency of 18.8% [2]) do not provide wearers with sufficient protection against the inhalation of virion-laden aerosols released by unmasked and infected individuals (Figure A.4).

The IPE of surgical masks vary across multiple literature [2, 4] (we choose the most conservative estimate to include in the main paper, but have evaluated across the range of efficiencies). Some recent work concluded that surgial mask has an IPE of 44% [4]. This can be attributed to the different properties of the surgical masks (fitting of and materials used for the masks) and the specific environment that such studies are conducted in [1]. Based on an IPE of 44%, the transmission risk that masked occupants face against the aerosols released by an unmasked and infected individual is shown in Figure A.5. With a slightly doubled IPE from the initial choice of 18.2%, the region of transmission risk generally decreases in size across the various scenarios. It is intuitive and apparent that higher IPE would be beneficial against an infection risk. Hence, masks with an improved IPE has been recently proposed with a higher IPE of 74% [1]. The use of face masks with an IPE of 74% provides the users with significantly more protection against unmasked SARS-CoV-2 carriers as compared to the existing surgical masks (Figure A.6).

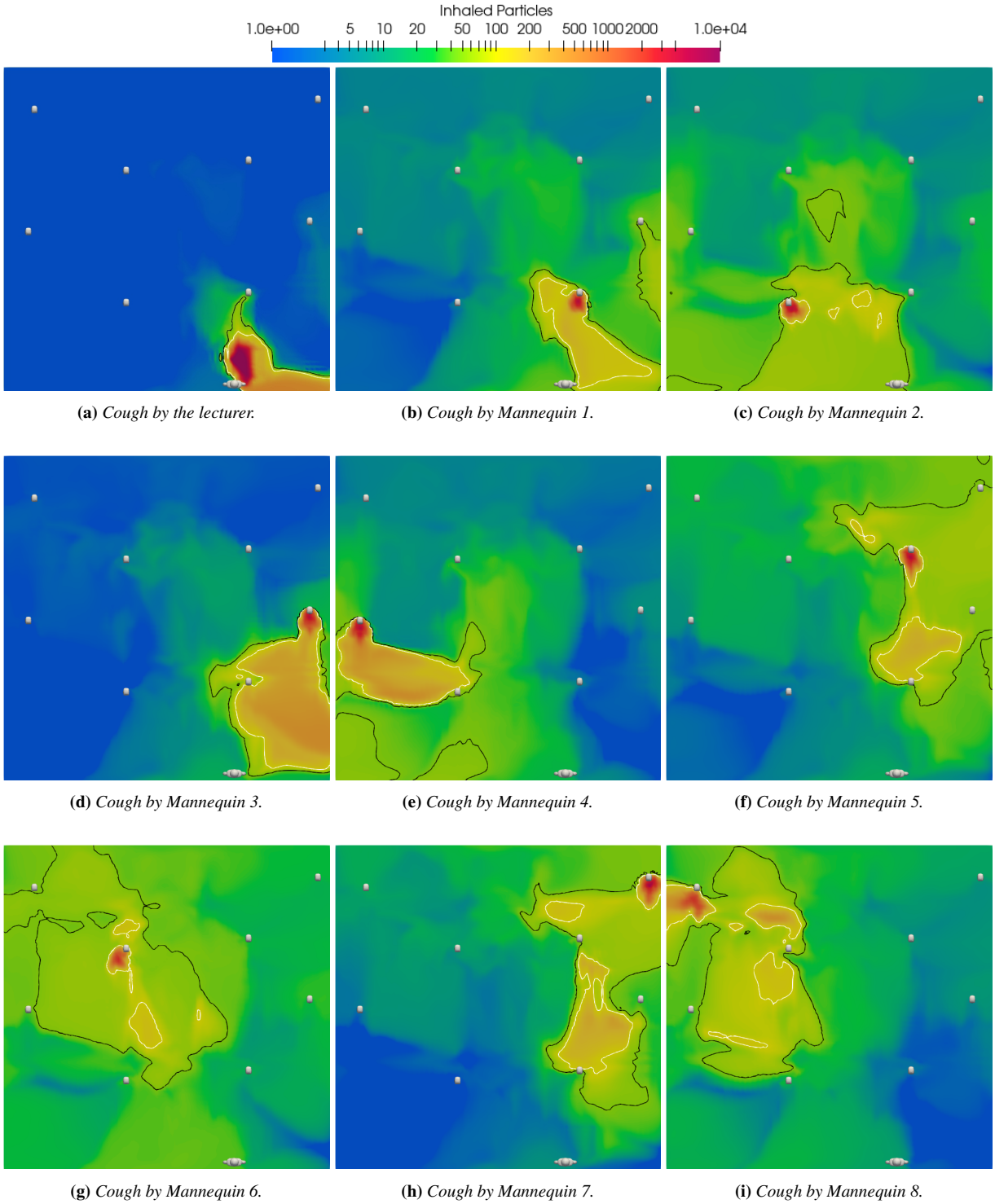

(a) *Cough by the lecturer.* **(b)** *Cough by Mannequin 1.* **(c)** *Cough by Mannequin 2.*

(d) *Cough by Mannequin 3.* **(e)** *Cough by Mannequin 4.* **(f)** *Cough by Mannequin 5.*

(g) *Cough by Mannequin 6.* **(h)** *Cough by Mannequin 7.* **(i)** *Cough by Mannequin 8.*

Figure A.3: *Contour of the transmission risk faced by the seated occupants due to the simulated coughs by the varied mannequins when everyone is unmasked*

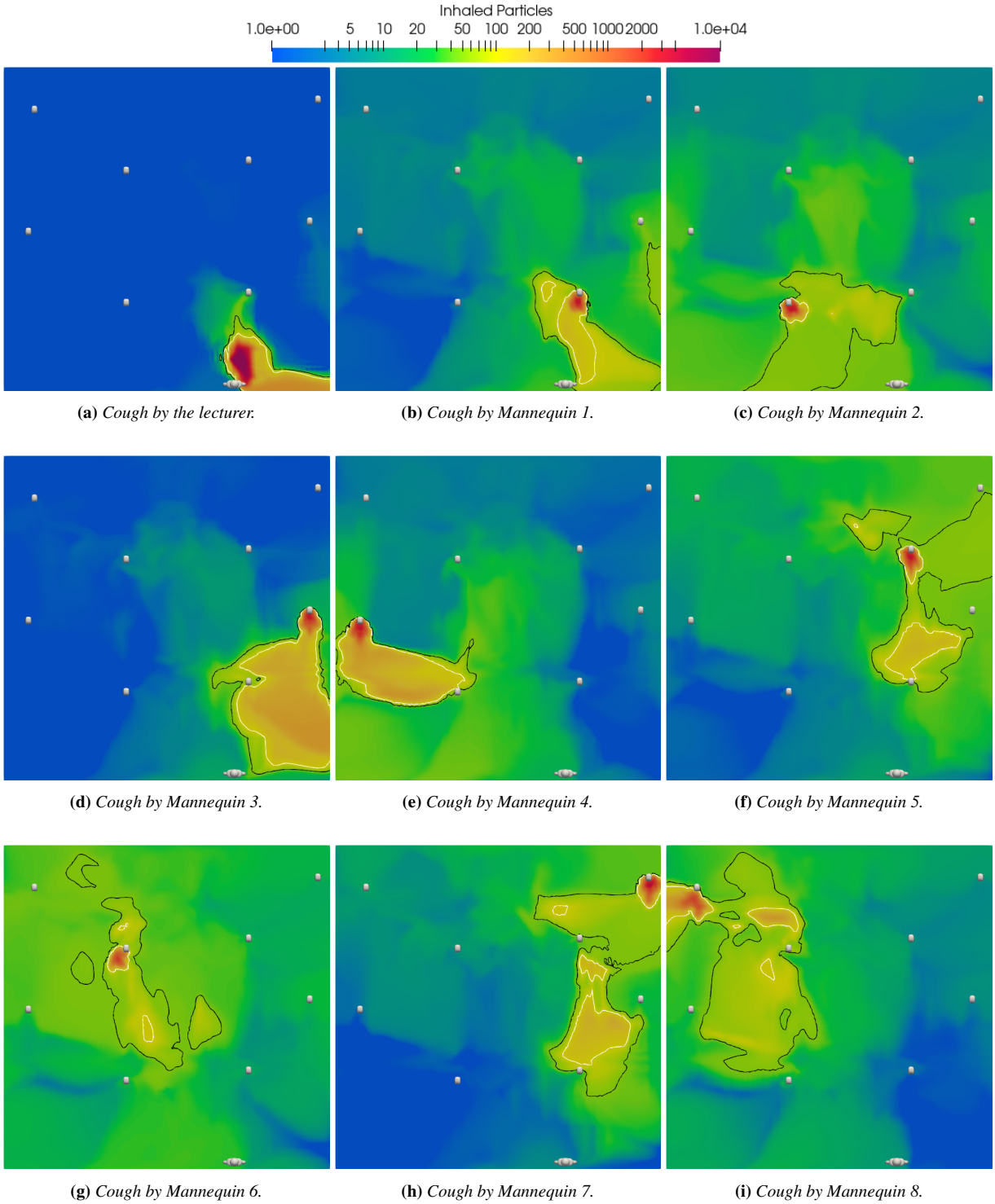

(a) *Cough by the lecturer.* **(b)** *Cough by Mannequin 1.* **(c)** *Cough by Mannequin 2.*

(d) *Cough by Mannequin 3.* **(e)** *Cough by Mannequin 4.* **(f)** *Cough by Mannequin 5.*

(g) *Cough by Mannequin 6.* **(h)** *Cough by Mannequin 7.* **(i)** *Cough by Mannequin 8.*

Figure A.4: *Contour of the transmission risk faced by the seated occupants (who are using face masks with 18.81% IPE) due to the simulated coughs by an unmasked mannequin*

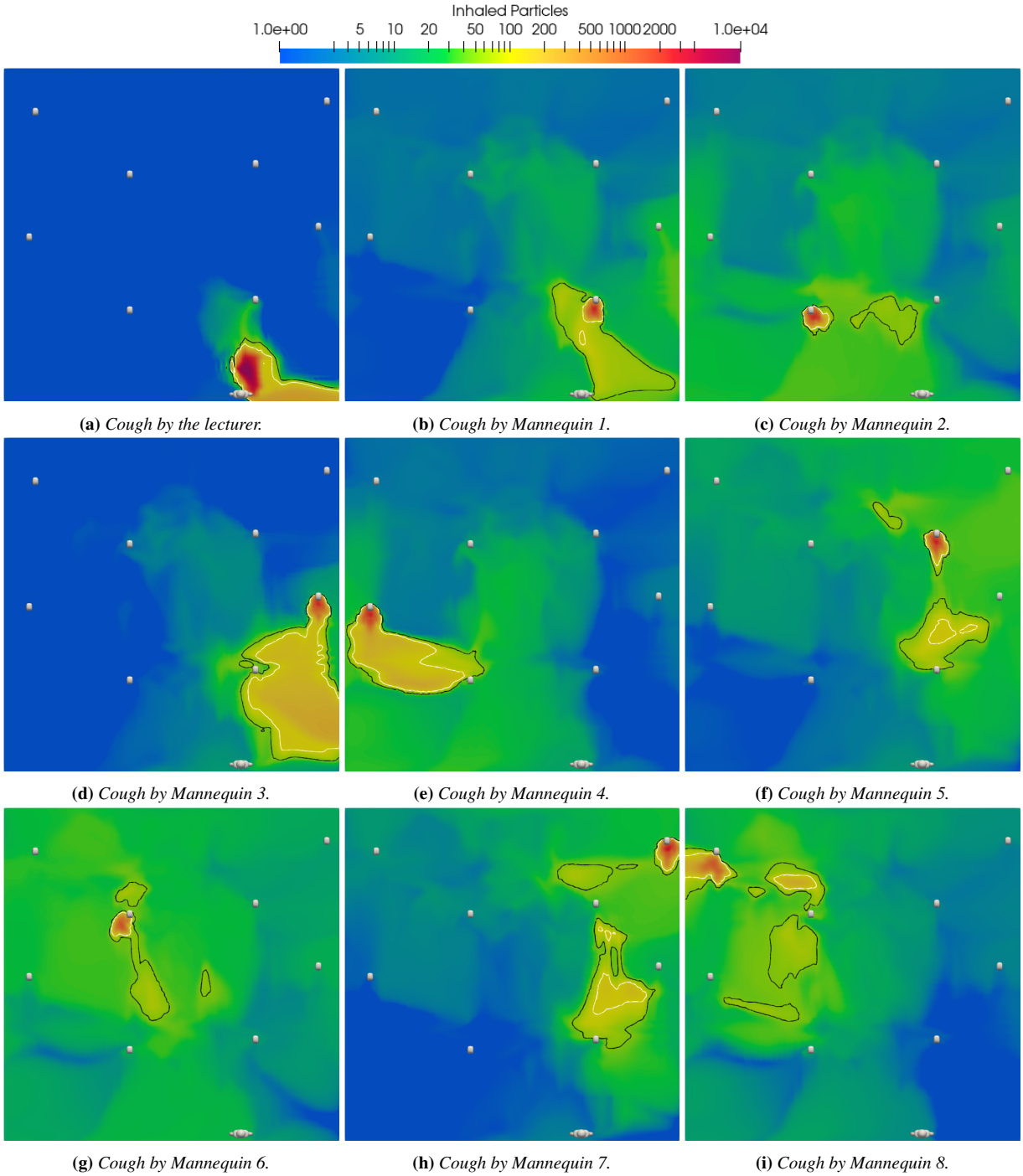

(a) *Cough by the lecturer.* **(b)** *Cough by Mannequin 1.* **(c)** *Cough by Mannequin 2.*

(d) *Cough by Mannequin 3.* **(e)** *Cough by Mannequin 4.* **(f)** *Cough by Mannequin 5.*

(g) *Cough by Mannequin 6.* **(h)** *Cough by Mannequin 7.* **(i)** *Cough by Mannequin 8.*

Figure A.5: *Contour of the transmission risk faced by the seated occupants (who are using face masks with 44% IPE) due to the simulated coughs by an unmasked mannequin*

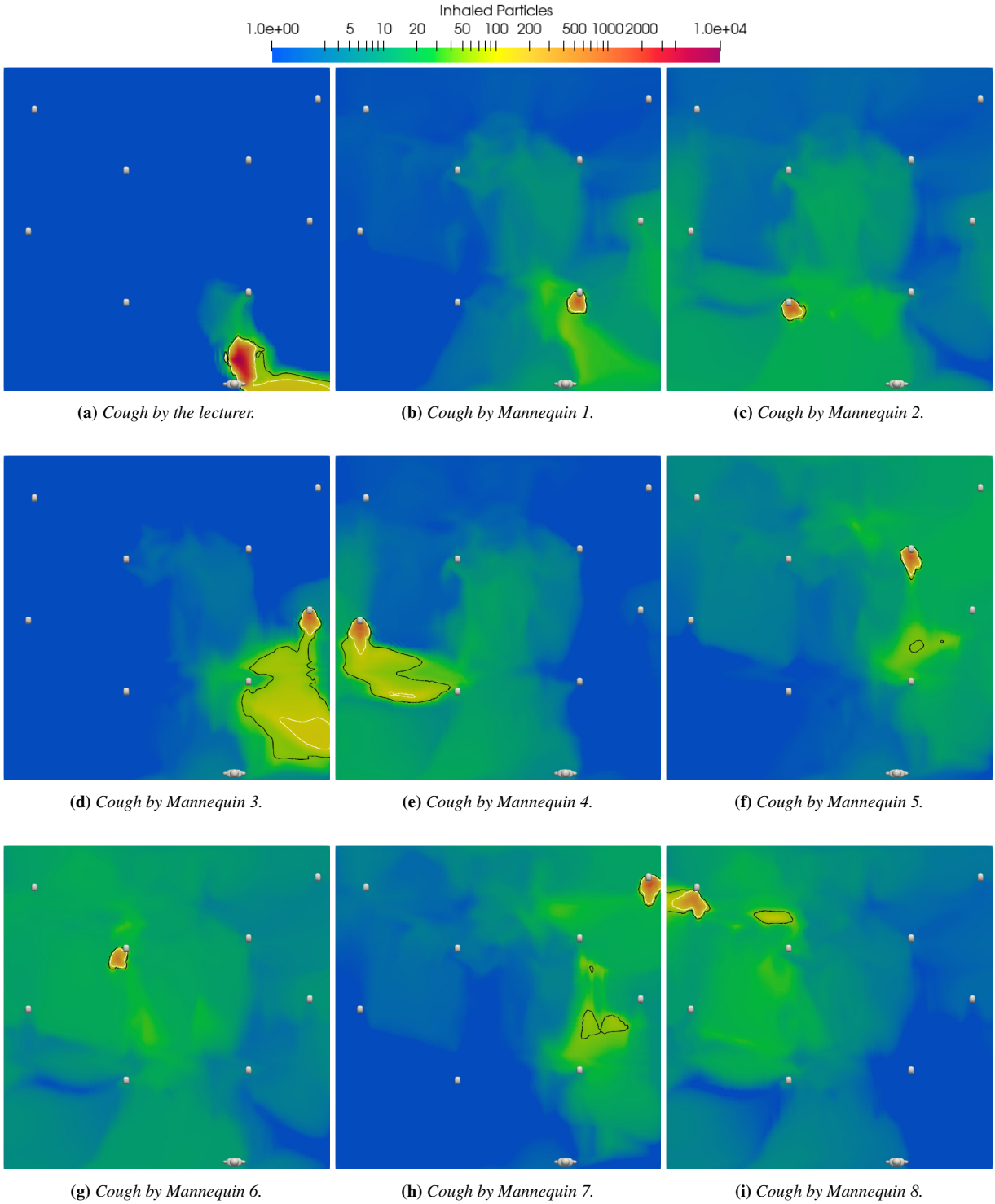

(a) *Cough by the lecturer.* **(b)** *Cough by Mannequin 1.* **(c)** *Cough by Mannequin 2.*

(d) *Cough by Mannequin 3.* **(e)** *Cough by Mannequin 4.* **(f)** *Cough by Mannequin 5.*

(g) *Cough by Mannequin 6.* **(h)** *Cough by Mannequin 7.* **(i)** *Cough by Mannequin 8.*

Figure A.6: *Contour of the transmission risk faced by the seated occupants (who are using face masks with 74% IPE) due to the simulated coughs by an unmasked mannequin*

B.2 Variation with MID

While the minimum infective dose (MID) has been hypothesized to be 50 for this paper [5], the actual MID for SARS-CoV-2 is still currently unknown. Hence, varying regions of transmission risk may be observed for different choices of MID (Figure A.7).

B.3 Risk Assessment of Lecturer

We can also conduct the transmission risk assessment on the standing mannequin (the lecturer). We can do this by analyzing a slice of the contour for the inhaled particle count taken at the height of $1.64m$, which corresponds to the location of the standing mannequin's breathing organs. The assessment concludes that the lecturer can still be affected by the coughs from the seated mannequins despite the social distancing guidelines (Figure A.8).

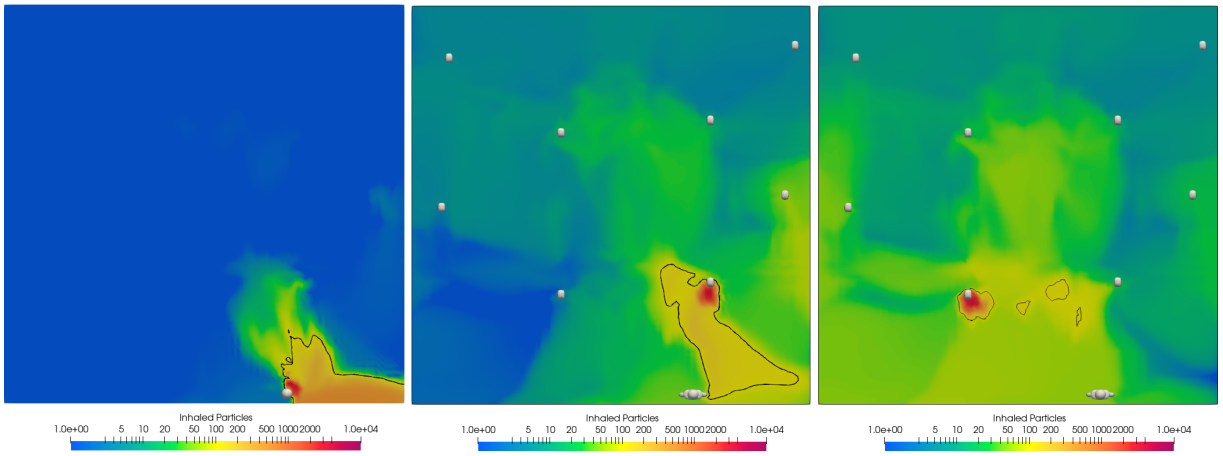

(a) *Cough by the lecturer.* **(b)** *Cough by Mannequin 1.* **(c)** *Cough by Mannequin 2.*

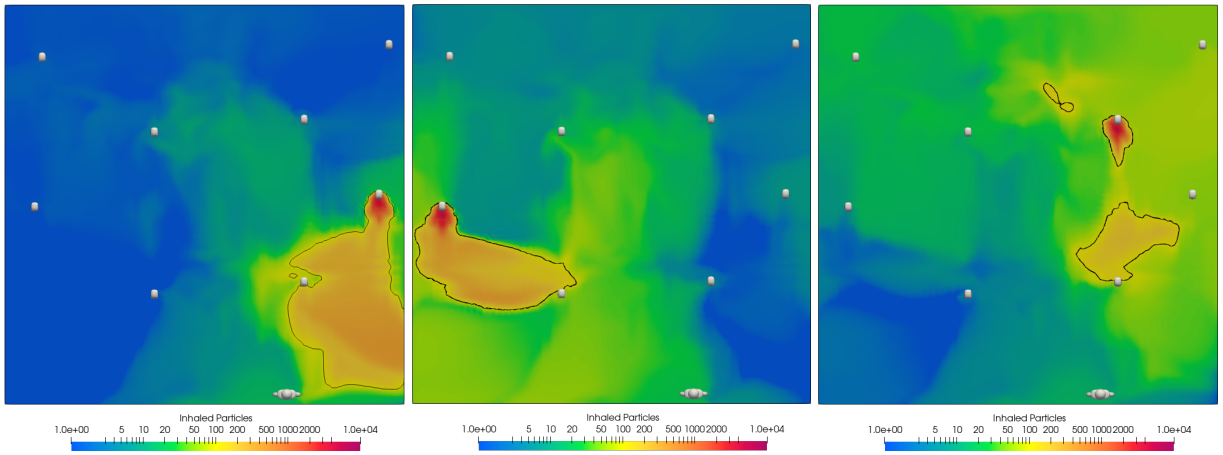

(d) *Cough by Mannequin 3.* **(e)** *Cough by Mannequin 4.* **(f)** *Cough by Mannequin 5.*

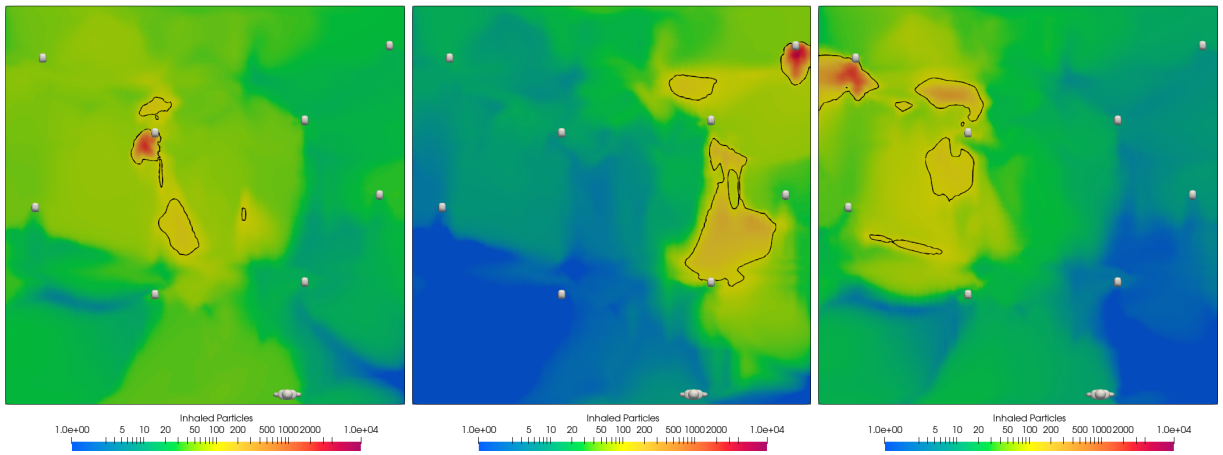

(g) *Cough by Mannequin 6.* **(h)** *Cough by Mannequin 7.* **(i)** *Cough by Mannequin 8.*

Figure A.7: *Contour of the transmission risk faced by the occupants due to the simulated coughs by the varied mannequins when everyone is unmasked with a more lenient choice of MID (MID=100)*

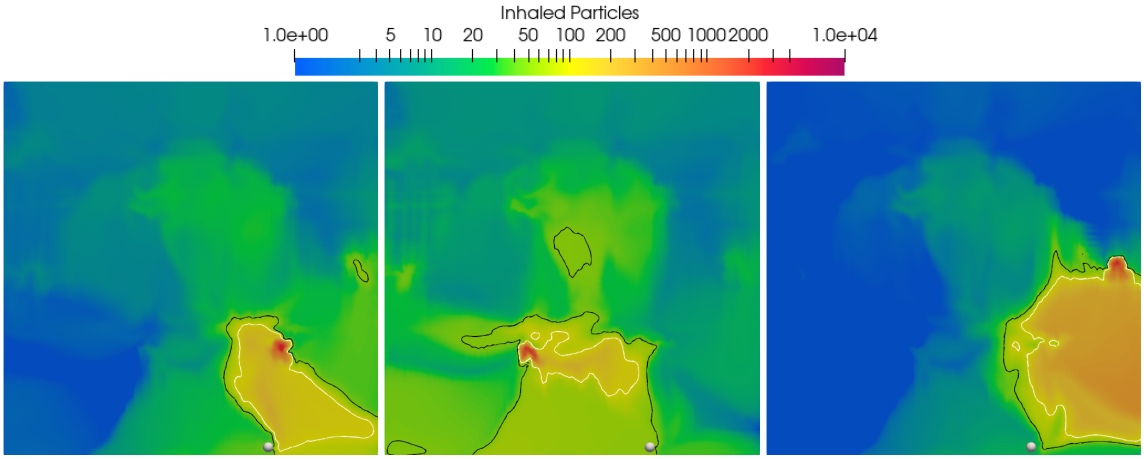

(a) *Cough by Mannequin 1.* **(b)** *Cough by Mannequin 2.* **(c)** *Cough by Mannequin 3.*

(d) *Cough by Mannequin 4.* **(e)** *Cough by Mannequin 5.* **(f)** *Cough by Mannequin 6.*

(g) *Cough by Mannequin 7.* **(h)** *Cough by Mannequin 8.*

Figure A.8: *Contour of the transmission risk faced by the standing occupant (lecturer) due to the simulated cough by the varied mannequins when everyone is unmasked*

References

[1] Jin Pan, Charbel Harb, Weinan Leng, and Linsey C. Marr. Inward and outward effectiveness of cloth masks, a surgical mask, and a face shield. *Aerosol Science and Technology*, 55(6):718–733, 2021. doi: 10.1080/02786826.2021.1890687.

[2] Mervin Zhao, Lei Liao, Wang Xiao, Xuanze Yu, Haotian Wang, Qiqi Wang, Ying Ling Lin, F. Selcen Kilinc-Balci, Amy Price, Larry Chu, and et al. Household materials selection for homemade cloth face coverings and their filtration efficiency enhancement with triboelectric charging. *Nano Letters*, 20(7): 5544–5552, 2020. doi: 10.1021/acs.nanolett.0c02211.

[3] Liqiao Li, Muchuan Niu, and Yifang Zhu. Assessing the effectiveness of using various face coverings to mitigate the transport of airborne particles produced by coughing indoors. *Aerosol Science and Technology*, 55(3):332–339, 2020. doi: 10.1080/02786826.2020.1846679.

[4] Abhiteja Konda, Abhinav Prakash, Gregory A. Moss, Michael Schmoldt, Gregory D. Grant, and Supratik Guha. Aerosol filtration efficiency of common fabrics used in respiratory cloth masks. *ACS nano*, 14(5):6339–6347, 2020.

[5] John M. Kolinski and Tobias M. Schneider. Superspreading events suggest aerosol transmission of SARS-CoV-2 by accumulation in enclosed spaces. *Phys. Rev. E*, 103(3):033109, 2021. doi: 10.1103/PhysRevE.103.033109.